DEPARTMENT OF PHYSICS

TECHNISCHE UNIVERSITÄT MÜNCHEN

Master's Thesis in Physics

Testing the Precision Optical Calibration Modules in the Gigaton-Volume-Detector

Kilian Holzapfel

December 14, 2018

Supervisor: Prof. Dr. Elisa Resconi

Second Assessor: Prof. Dr. Lothar Oberauer

Abstract

The initial idea of the Precision Optical CAlibration Modules (POCAM) is to reduce the uncertainties in IceCube. The development and the specification of this module are summarized in this thesis. Furthermore, the data from testing the POCAM in a cluster of the Gigaton Volume Detector (GVD) are presented and analyzed. The energy measured by the in-situ monitoring of the POCAM and by the cluster array show proportionality. Besides, optical properties of the water, namely the refractive index and attenuation length have been verified. Moreover, the detector geometry could be calibrated. The number of events and the missing insight to GVD as well as no possibilities for a cross-check reduces the significance of this analysis.

Zusammenfassung

Die ursprüngliche Idee des Precision Optical CAlibration Modul (POCAM) war und ist die Verringerung der Unsicherheiten des IceCube-Detektors. Die Entwicklung und Spezifizierung des Moduls ist in dieser Arbeit zusammengefasst. Des Weiteren werden die Daten, die durch den Test des POCAM in einer Untergruppe des Gigaton Volume Detektor (GVD) gesammelt wurden, präsentiert und ausgewertet. Mit Hilfe der Daten der Sensoren für die Selbst-Kalibrierung des POCAM und den Daten des GVD konnte ein proportionaler Zusammenhang der gemessenen Energie festgestellt werden. Außerdem konnten der Brechungsindex und Abschwächungslänge für das Wasser des Detektors verifiziert werden. Zusätzlich war es möglich, die Geometrie des Detektors zu messen. Die geringe Anzahl an Events, der fehlende Einblick in GVD und die fehlende Möglichkeit einer anderweitigen Überprüfung der Ergebnisse, reduziert die Aussagekraft dieser Analyse.

Contents

Contents

List of Figures

List of Tables

List of Tables

1 Neutrino Physics

Neutrino physics is largely an art of learning a great deal by observing nothing.

(Haim Harari, 1988)

In 1930 Wolfgang Pauli described the neutrino (ν) as an 'apology' for the apparent non-conservation of energy and momentum in β-decay. He thought it was "a terrible thing" to postulate "a particle that cannot be detected." Four years later H.A. Bethe and R.E. Peierls calculated with Fermi's theory an absorption length in light years of lead. At this point, a detection had to be declared as impossible with the existing neutrino sources and the technology for detectors. In fact, it took nearly three decades until Cowan and Raines observed the first electron antineutrino ($\bar{\nu}_e$) in 1956. And some more years, to detect the muon neutrino (ν_μ) by L. Lederman, M. Schwartz and J. Steinberger in 1962. Finally, in 2000, the tau neutrino (ν_τ) by the *DONUT* experiment was discovered [10, 26].

As the extreme small cross-section is creating the biggest problem for neutrino experiments, it is also the characteristic which is appreciated in the astrophysics. In contrast to photons, neutrinos can travel the distance between the nuclei of an astronomical event and the earth without interactions. This creates a unique insight into the underlying processes of astrophysical phenomena. In this way, the first contribution of neutrinos was to prove the fusion process inside the sun — a measurement which also gave evidence about an idea in particle physics of neutrino oscillation.

Today a high number of experiments pushes on the knowledge in neutrino physic. Nearly all of them have to find solutions for the ultra-low rate of the aimed reactions, which tend towards huge, massive and highly shielded experiments. But there are still open questions on fundamental characteristics of neutrinos, and the astronomy with neutrinos has just started [19].

1.1 The Standard Model

After a long way of experiments and theories, the Standard Model (SM) of particle physics was developed in the second half of the 20th century. It includes the strong, weak and electromagnetic interaction with the five corresponding gauge bosons as well as the mass-generating Higgs boson and all known fermions. An illustration of all particles with basic characteristics in the SM is shown in Figure 1.1.
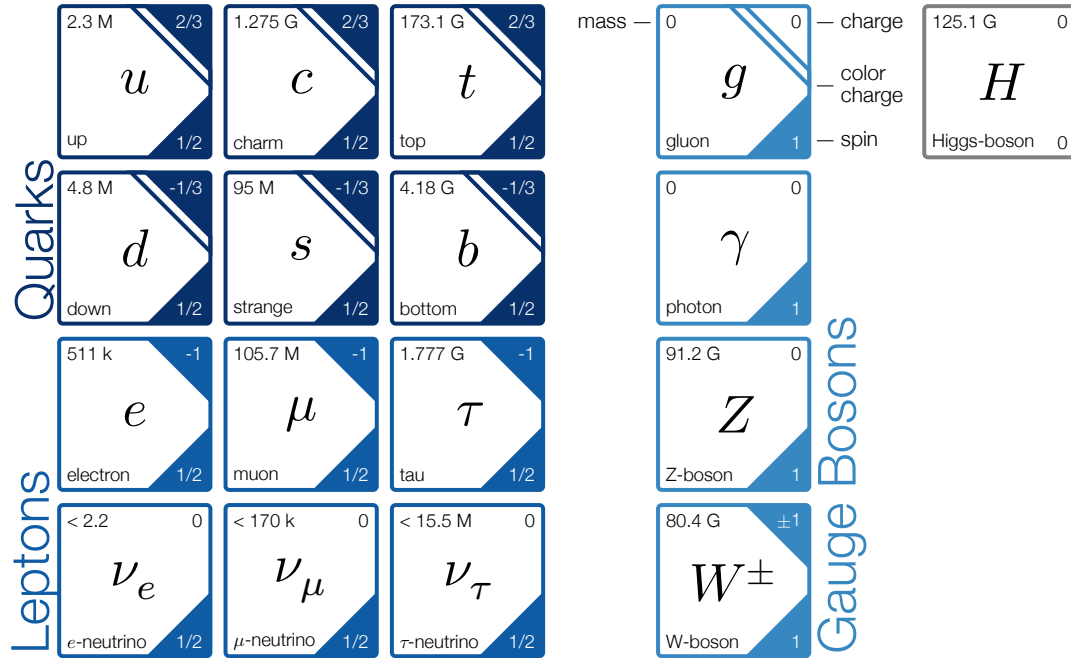
Figure 1.1: *Schematic depiction of the Standard Model of particle physics, with the three generation of fermions column 1-3), gauge bosons (column 4), Higgs boson (column 5), Quarks (dark blue) and Leptons (blue). The mass (top left), charge (top right), spin (bottom right), color charge (extra diagonal line) is listed for every particle . Inspired by [8]*

The gauge symmetries are described by

$$G_{SM} = SU(3) \times SU(2) \times U(1) \tag{1.1}$$

with the strong, weak and electromagnetic group respectively. Each Interaction couples to one property of the particles and is mediated by specific gauge bosons. Table 1.1 summarizes the characteristics of the three interactions plus the gravitational interaction. The strong interaction couples to the color charge with the eight different gluons (g) as mediators. Among the fermions, only quarks have a color charge and can be affected by the strong interaction. In a range of 10^{-15} m it is approximately 137 times stronger than the electromagnetism, and it confines quarks to hadron particles and binds neutrons and protons to create atomic nuclei.

The electromagnetic interaction couples to the (electric) charge with the photon (γ) as mediator. Quarks, the electron (e^-), the muon (μ^-) and the tau (τ^-) are the (electric) charged fermions which can be forced by the electromagnetic interaction. It is the force which binds electrons to atomic nuclei as well as atoms to molecules and defines the main features of everyday objects.

The weak interaction couples to the flavor with the mediator Z^0 and $W^\pm$. It is the weakest of the three forces with the lowest range but takes effect to all leptons including the three neutrino flavors (ν_e, ν_μ, ν_τ). Among others, it results in beta decay and is the primary interaction for all neutrino reactions [28].

Table 1.1: *Overview of basic characteristics of the four fundamental interactions. The listed gravity with the hypothetical graviton is not included in the SM [28].*

Interaction	Strength	Range [m]	Source	Mediator Particle	Mass [GeV c^{-2}]	Affected Fermions
Strong	~1	10^{-15}	color	gluon	0	Q
Electromagnetic	~1/137	∞	ele. charge	photon	0	Q, e, μ, τ
Weak	~10^{-5}	10^{-18}	flavor	$W^{\pm}, Z^0$	80, 91	Q, e, μ, τ, ν
Gravity	~10^{-38}	∞	mass	*graviton*	0	Q, e, μ, τ, ν
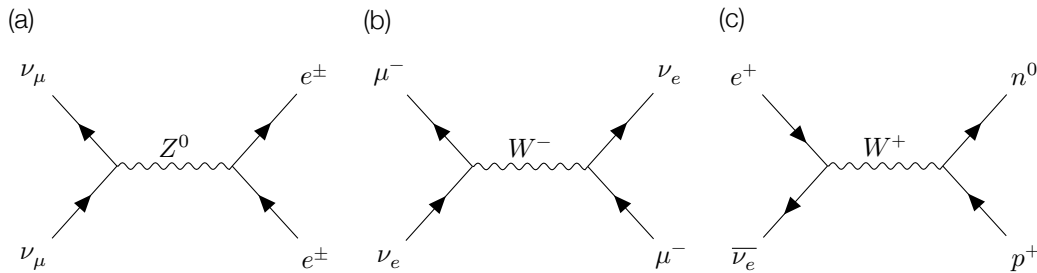
Figure 1.2: *Feynman diagrams of three weak interaction processes. (a) Scattering of a moun neutrino at an electron, where no particle are converted. As it is mediated by a Z^0, this is a neutral current (NC) interaction. (b) But scattering is also possible via a charged current (CC) interaction where a $W^{\pm}$ is exchanged. (c) Another charged current interaction is the inverse beta decay. The reaction of an electron antineutrino scattering with a proton, creating a positron and a neutron. More elementary, this interaction changes an Up-quark (u) into a Down-quark (d), which results in the change of the proton $(u - u - d)$ to a neutron $(u - d - d)$.*

1.1.1 Weak Interaction

As the weak interaction is coupling to the flavor of a particle, it is the only force which can cause a change of the involved particles, shown in Figure 1.2 (c). Like summarized in Table 1.1, the strength of the weak interaction is approximately 10^{-5} lower than the strong interaction. Also, its range, of about 10^{-18} m, is three magnitudes lower, compared to the strong interaction or the radius of the proton. Both characteristics result from the high masses of the gauge bosons, mediating the weak interaction. Furthermore, it is the reason why the cross section and interaction rate for weak interactions are sometimes so small. And the reason why an observation of weak interactions is so laborious.

Determined by the charge of the involved gauge bosons, the weak force has two ways of interactions. The uncharged Z^0-boson and the charged $W^{\pm}$-bosons are mediating the neutral currents (NC) and charged currents (CC) respectively. Feynman diagrams for both currents are illustrated in Figure 1.2.

In the Standard Model, the CC and the NC are described by the Lagrangians

$$-\mathcal{L}_{CC} \sim \frac{g}{2\sqrt{2}} W_\mu^+ \bar{\nu}_\alpha \gamma^\mu \left(1-\gamma^5\right) l_\alpha^- + h.c. \tag{1.2}$$

$$-\mathcal{L}_{NC} \sim \frac{g}{\cos\left(\Theta_W\right)} \left(\frac{1}{2}\bar{f}_\alpha \gamma^\mu \left(1-\gamma^5\right) f_\alpha + \sin\left(\Theta_W\right)^2 \left(\bar{l}_\alpha \gamma^\mu l_\alpha\right)\right) Z_\mu \tag{1.3}$$

with the flavor $\alpha \in \{e, \mu, \tau\}$, the coupling constant g, the gamma matrices γ^μ with $\gamma^5 = i\gamma^0\gamma^1\gamma^2\gamma^3\gamma^4$, fermion field f, neutrino field ν, lepton field l, the weak mixing angle (Weinberg angle) Θ_W and the weak boson fields Z_μ and W_μ^+.

The Lagrangian of the neutral current ($\mathcal{L}_{NC}$) allows an interaction with left- and right-handed fermions or anti-fermions. Whereas the Lagrangian of the charged current ($\mathcal{L}_{CC}$) has only a therm with the left-handed projection operator $P_L = \frac{1-\gamma^5}{2}$, which allows only left-handed fermions or right-handed anti-fermions. In other words the CC violates the *charge conjugation* (C) and the *parity* (P). Furthermore, the combination of both (CP) is also violated by the weak interaction, which was observed in the decay of kaons in 1964 [25].

Neutrinos can only be created or annihilated by the CC, which means that there are only left-handed neutrinos or right-handed antineutrinos. As the momentum of every massive particle can be reversed by a Lorentz boost of the frame of reference, neutrinos in the SM were assumed to be massless and travel with c. However, neutrino oscillation has been detected, implying neutrinos are not massless [16].

1.1.2 Beyond the Standard Model

In the past decades, the Standard Model became the most important framework of particle physics. The SM was even able to make theoretical predictions, which have been proven by experiments later. However, some fundamental questions remain unanswered in the SM. For example, why are there four fundamental forces rather than one and why are the properties of the four so different? How can the gravity be included? Why is our universe mainly out of matter and not anti-matter? Is the fractional charge of the quarks related to color? Which effect is generating the mass of neutrinos?

In theoretical physics, the primary goal is to formulate a theory with all four fundamental forces and observations, so-called *grand unification theories*, or GUT. Approaching these questions experimentally will require more advanced detectors than currently existing around the world [28].

1.2 Neutrino Oscillation

In 1957 Bruno Pontecorvo published the idea of the theoretical possibility that a "*neutrino*" to "*antineutrino transitions could take place in vacuo*" [24]. Some years later the *Homestake-Experiment* detected one-third of the predicted neutrino flux from the sun [9]. First classified as an incorrect solar model or a wrong measurement, later the neutrino oscillation was identified as the only possible

reason for the missing flux [27].

This observation leads to mainly two conflicts with the Standard Model. Most obviously, the oscillation violates the lepton number conservation. Second, neutrinos have a non-zero mass, and therefore they are not propagating in the vacuum with the speed of light which allows the existence of right-handed neutrinos generated by the weak interaction in the combination of a Lorentz boost.

1.2.1 Vacuum Oscillation

Neutrinos at the weak interaction are labeled by the three flavors or flavor eigenstates $\nu_\alpha, \alpha \in \{e, \mu, \tau\}$. However, in theory, the propagation is related to the mass eigenstates $\nu_k, k \in \{1, 2, 3\}$ with the Hamiltonian. Both types are linked because every flavor eigenstate is a linear combination of all mass eigenstates and vice versa.

$$|\nu_\alpha\rangle = \sum_k U_{\alpha k} |\nu_k\rangle \tag{1.4}$$

$$|\nu_k\rangle = \sum_\alpha U_{\alpha k}^* |\nu_\alpha\rangle \tag{1.5}$$

$U_{\alpha i}$ are the matrix elements of the *Pontecorvo-Maki-Nakagawa-Sakata matrix* (PMNS)

$$U = \begin{pmatrix} 1 & 0 & 0 \\ 0 & c_{23} & s_{23} \\ 0 & -s_{23} & c_{23} \end{pmatrix} \begin{pmatrix} c_{13} & 0 & s_{13}e^{-i\delta} \\ 0 & 1 & 0 \\ -s_{13}e^{-i\delta} & 0 & c_{13} \end{pmatrix} \begin{pmatrix} c_{12} & s_{12} & 0 \\ -s_{12} & c_{12} & 0 \\ 0 & 0 & 1 \end{pmatrix} \tag{1.6}$$

with $s_{kj} = \sin(\theta_{kj})$, $c_{kj} = \cos(\theta_{kj})$, the weak mixing angle θ_{kj} and the CP violating phase δ. The propagation in vacuum is described by the time-dependent Schrödinger equation with the Hamiltonian H and the mass eigenstates $|\nu_k\rangle$ and $H|\nu_k\rangle = E_k |\nu_k\rangle$.

$$i\hbar \frac{\partial}{\partial t} |\nu_k(t)\rangle = H_0 |\nu_k\rangle \tag{1.7}$$

As the neutrino mass is very small $m_k << E_k$ and by introducing a mass-dependent phase

$$\Phi_k := \frac{m_k^2 c^4}{2p^2 c^2} \tag{1.8}$$

the energy-momentum relation can be simplified with

$$\sqrt{1+x} = 1 + \frac{x}{2} + \mathcal{O}(x^2) \text{ at } x \approx 0 \tag{1.9}$$

and $p_k \approx p$, $\forall k$ to

$$E_k = \sqrt{p_k^2 c^2 + m_k^2 c^4} \tag{1.10}$$

$$\approx p_k c + \frac{m_k^2 c^4}{2p_k^2 c^2}$$

$$\approx pc + \Phi_k \tag{1.11}$$

Neutrino Oscillation

A solution of eq. (1.7) is a plan wave

$$|\nu_k(t)\rangle = e^{-\frac{i}{\hbar}pct}e^{-\frac{i}{\hbar}\Phi_k t}|\nu_k\rangle \tag{1.12}$$

Combining eq. (1.4), eq. (1.5) and eq. (1.12) gives the time-dependent transmission amplitude of a flavor change from α to β with the orthogonality $\langle\nu_j|\nu_k\rangle = \delta_{kj}$

$$\langle\nu_\beta(t)|\nu_\alpha\rangle = \sum_j \sum_k U^*_{\beta j}e^{-\frac{i}{\hbar}pct}e^{-\frac{i}{\hbar}\Phi_k t}U_{\alpha k}\langle\nu_j|\nu_k\rangle$$

$$= e^{-\frac{i}{\hbar}pct}\sum_k U^*_{\beta k}e^{-\frac{i}{\hbar}\Phi_k t}U_{\alpha k} \tag{1.13}$$

Adding the distance L from the neutrino source to the detection with $L = ct$, the squared amplitude yields the probability function of a transition after a distance L

$$P_{\alpha\to\beta}(t) = \left|\langle\nu_\beta(t)|\nu_\alpha\rangle\right|^2$$

$$= \delta_{\alpha\beta}$$

$$- 4\sum_{k>j}\mathcal{R}e\left(U^*_{\alpha j}U_{\beta j}U_{\alpha k}U^*_{\beta k}\right)\sin^2\left(\frac{\Delta m^2_{kj}c^4 L}{4E\hbar c}\right)$$

$$+ 2\sum_{k>j}\mathcal{I}m\left(U^*_{\alpha j}U_{\beta j}U_{\alpha k}U^*_{\beta k}\right)\sin\left(\frac{\Delta m^2_{kj}c^4 L}{2E\hbar c}\right) \tag{1.14}$$

with the squared mass difference $\Delta m^2_{kj} = m^2_k - m^2_j$. If the mass eigenstates have a different mass and therefore also a non-zero mass, eq. (1.14) shows that there is a probability to observe a different flavor after a propagation distance. This function is plotted in Figure 1.3 which shows why this effect is called *neutrino oscillation*. [15]

1.2.2 Mass Hierarchy

Neutrino oscillation experiments can measure the properties of eq. (1.14) which are the mixing angles Θ_{kj} and the squared mass difference Δm^2_{kj}. However, they are not sensitive to the absolute mass scale. Hence, a significant question is the neutrino mass hierarchy.

However, the sign of the mass splitting Δm_{12} has been determined by using matter effects of the solar neutrinos in the earth. Which leave two possibilities for the neutrino hierarchy, the so-called *normal* (NH) or *inverted* (IH) hierarchy, with

$$m_1 < m_2 < m_3 \quad (NH)$$
$$m_3 < m_1 < m_2 \quad (IH)$$

or visualized in Figure 1.4.
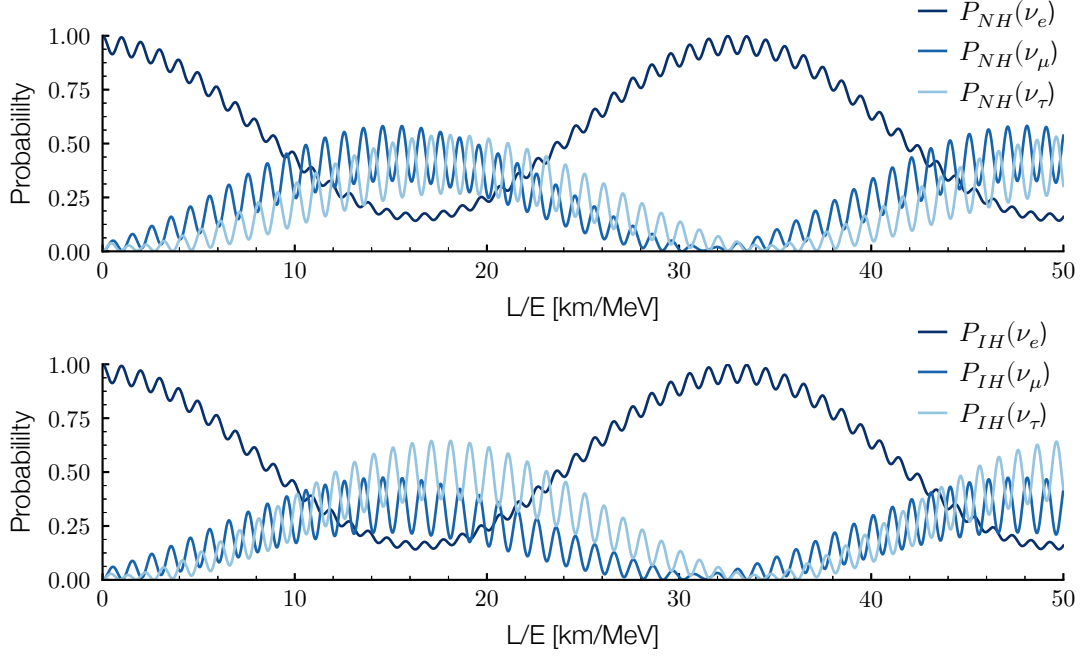
Figure 1.3: *Neutrino oscillation in vacuum calculated with the eq. (1.14) and the best fit values from [23]. The initial flavor is a electron neutrino ν_e and the $P(\nu_\alpha)$ shows the probability to detect the flavor α in dependency of distance per energy in [km/MeV] and the normal hierarchy NH (top) as well as the inverted hierarchy IH (bottom).*

1.2.3 Matter Effects

Neutrinos can penetrate astronomical objects like stars with only a small absorption, due to the quasi-infinitesimal cross-section. However, the matter is influencing the neutrino oscillation, and this effect was used to determine the sign of Δm_{12} like mentioned in subsection 1.2.2.

As shown in section 1.2, the oscillation is the result of a phase difference of the mass eigenstates ν_k. If neutrinos propagate through matter, the flavor eigenstates ν_α can scatter at the matter over the weak interaction. From a ν_k, the portion of all three flavor eigenstates can do this over the NC channel, but only ν_e can scatter with e^- though CC interactions. This shifts the energy levels of the mass eigenstates because ν_e is a linear combination of all three ν_k. Therefore, neutrinos in matter have a different effective mass than in vacuum. Since the oscillation is related to the square of the mass differences, matter can influence the oscillation. In the Hamiltonian, this is expressed by a potential $V = \sqrt{2} G_F n_e$

$$H = H_0 + V \tag{1.15}$$

with the *Fermi coupling constant* G_F and the electron number density in the matter n_e. The time-
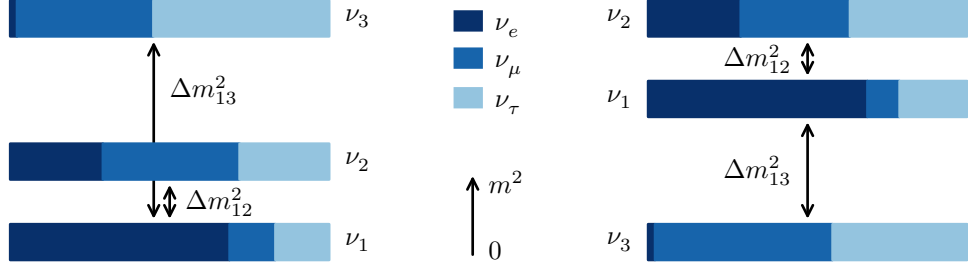
Figure 1.4: *The normal (left) or inverted (right) neutrino mass hierarchy with the flavor $\nu_\alpha, \alpha \in \{e, \mu, \tau\}$ composition of the mass eigenstates $\nu_k, k \in \{1,2,3\}$. For this visualization the best fit values from [23] have been used.*

dependent Schrödinger equation result in a non-trivial differential equation

$$
i\frac{\partial}{\partial t}\begin{pmatrix} \nu_e \\ \nu_\mu \\ \nu_\tau \end{pmatrix} = \left[\frac{1}{2E} U \begin{pmatrix} m_1^2 & 0 & 0 \\ 0 & m_2^2 & 0 \\ 0 & 0 & m_3^2 \end{pmatrix} U^\top + \begin{pmatrix} V & 0 & 0 \\ 0 & 0 & 0 \\ 0 & 0 & 0 \end{pmatrix} \right] \begin{pmatrix} \nu_e \\ \nu_\mu \\ \nu_\tau \end{pmatrix} \tag{1.16}
$$

with the PMNS matrix as U from eq. (1.6). For the two flavors case, this can be simplified to

$$
i\frac{\partial}{\partial t}\begin{pmatrix} \nu_e \\ \nu_\mu \end{pmatrix} = \frac{\Delta m^2}{4E} \begin{pmatrix} -\cos(2\theta_m) + V & \sin(2\theta_m) \\ \sin(2\theta_m) & \cos(2\theta_m) \end{pmatrix} \begin{pmatrix} \nu_e \\ \nu_\mu \end{pmatrix} \tag{1.17}
$$

which evolves in an oscillation probability of

$$
P_{e\to\mu}(L) = \sin^2(2\theta_m)\sin^2\left(\frac{\Delta m_m^2 L}{4E}\right) \tag{1.18}
$$

where θ_m and Δm_m^2 are the mixing parameters and the mass differences in matter. The matter parameters can also be expressed with

$$
\sin^2(2\theta_m) = \frac{\sin^2(2\theta)}{\left(\cos(2\theta) - \frac{2E}{\Delta m}V\right)^2 + \sin^2(2\theta)} \tag{1.19}
$$

$$
\Delta m_m^2 = \Delta m^2 \sqrt{\left(\cos(2\theta) - \frac{2E}{\Delta m}V\right)^2 + \sin^2(2\theta)} \tag{1.20}
$$

and for $V \to 0$ matter and vacuum get equal $\theta_m = \theta$, $\Delta m_m^2 = \Delta m^2$. [22]

Maximize the equation eq. (1.19) gives the *Mikheyev-Smirnov-Wolfenstein* (MSW) resonance condition

$$
\cos(2\theta) = \frac{2E}{\Delta m^2}V
$$

$$
\frac{\Delta m^2}{2E}\cos(2\theta) = \sqrt{2}G_F n_e \tag{1.21}
$$

with $\sin^2(2\theta_m) = 1$ or e.g. $\theta_m = \frac{\pi}{2}$. This means that, independent from a small vacuum mixing angle, the mixing angle in matter and the transition probability can be large, if the MSW condition is fulfilled. Another resonance effect in matter is the *parametric enhancement*. This resonance appears when neutrinos propagate through a certain periodic density pattern of matter. For both effects and the matter effect itself, more informations can be found in [2, 21, 22].

Neutrino Oscillation

2 Gigaton Volume Detector

Around 640 km long, 50 km wide and up to 1642 m deep, Lake Baikal is not only the deepest lake on earth, but it is also the most abundant liquid freshwater reservoir with nearly a quarter of the world's fresh surface water and more than the North American Great Lakes combined. It is considered to be the oldest [18] and the clearest [20] lake on earth.

This water properties make Lake Baikal to a suitable environment for a neutrino telescope. Therefore the Gigaton Volume Detector (GVD) is currently under construction and will instrument 1 km^3 of this clear water at a depth of 750 m to 1275 m. An array out of Optical Modules (OMs) measures Cherenkov light, emitted by relativistic charged particles passing the water. These particles can be secondary particles of neutrino reactions if a neutrino with enough energy interacts with the water inside or close to the detector.

Former test detectors at the same location have been deployed successfully and have been able to measure neutrinos. However, they also showed, that the optical properties of the water are not excellent [7].

Figure 2.1: *The view from a mountain northeast of shore station, taken during the deployment in March 2017. The detector has its location approximately 4 km from shore and it is deployed during February and March when the lake is frozen. This picture shows the deployment station (left) and the shore station with data acquisition center (lower right).*
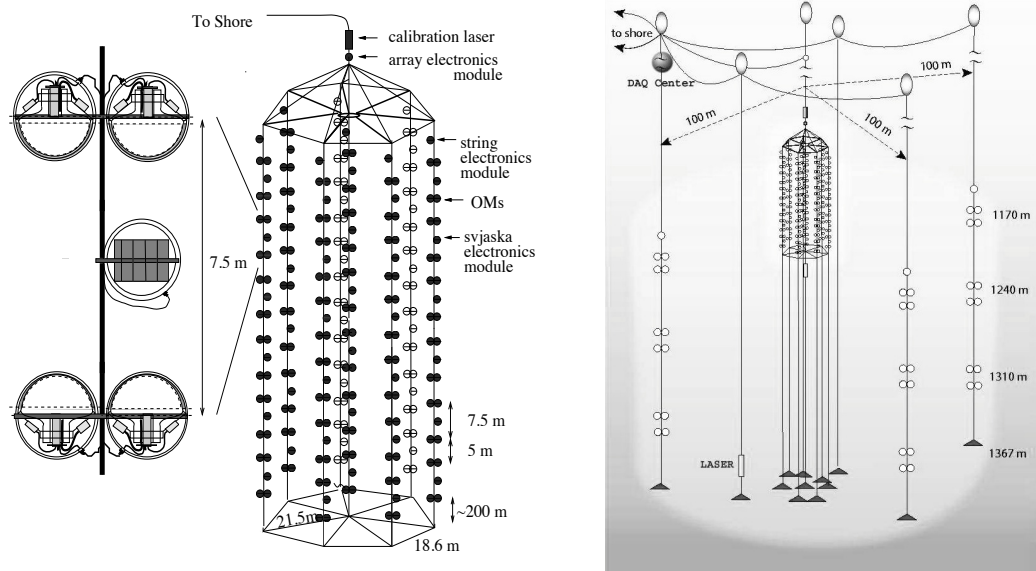
Figure 2.2: *The geometry of the detector NT200 (left) in 1998 and its upgrade NT200+ (right) in 2005. The expansion on the left shows four pairwise mounted optical modules (OMs) and in the middle an electronic module which hosts parts of the read-out and control electronics. For the upgrade NT200+, three additional strings have been deployed around the old NT200. Figures are exported from [6, 7].*

In winter 2017 two clusters with a total number of 16 strings have been deployed. As a part of it, the Precision Optical Calibration Module (POCAM) was included for testing the module itself and the capability of helping to calibrate a detector like GVD. After one year and several tests runs the POCAM was safely recovered in March 2018.

2.1 History

Since the early 90s, Lake Baikal is playing a role in neutrino physics. It all started with the NT200 detector, shown in Figure 2.2. The detector reached the final size of 8 strings with 192 pairwise grouped optical modules (OMs) in 1998. With a inter-string spacing of 21.5 m and a hight of 72 m, the detector instruments a mass of $\sim$30 000 t in a depth of 1100 m to 1170 m [6].

In the first five years (April 1998 till February 2003) NT200 had a operating time of $\sim$60 % or 1038 days. During this time it recorded $3.45 \cdot 10^8$ events with a minimum of 4 OM-hits, out of which 372 upward going muon neutrino ν_μ events have been found [6, 7, 30].

In 2005 the detector was upgraded to NT200+ with three additional strings placed 100 m around the current detector. The three strings increase the sensitivity for high energy neutrinos by a factor of 4. Each string has 12 pairwise grouped OMs mounted over a total length of 140 m with a spacing of 20 m to 50 m. The vertical position from 1170 m to 1310 m is a bit deeper than the NT200 core.
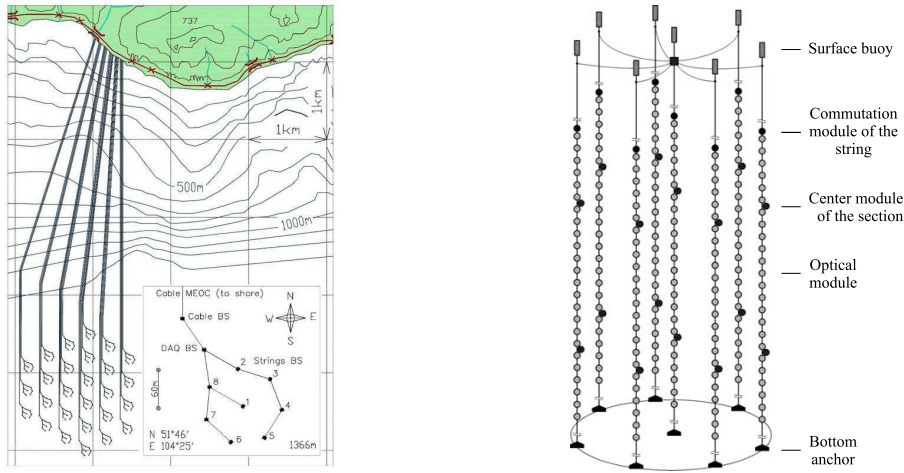
Figure 2.3: *In the final stage, the GVD detector consists out of 27 independent cluster, where every cluster has its own connection to shore (left). Each cluster (right) has 8 strings, placed in a heptagon with 60 m radius and one string at the center. The 36 OMs per string have a vertical spacing of 15 m and are separated in three sections [3, 5].*

Both detectors, NT200 and NT200+, are prototypes for a km^3-scale neutrino telescope called Baikal Gigaton Volume Detector (GVD) which will be located at the same location. The construction of GVD started with the test array Dubna in 2015. Once finished it will be the most northern km^3-scale neutrino telescope [6].

2.2 Design and Geometry

The Baikal-GVD is a 3-dimensional array of photomultiplier covering a volume of 1 km^3. It is located in the south-eastern part of Lake Baikal at a distance of 3.6 km with the coordinates 51°45′54″ N and 104°25′1″ E. At this location there is a flat basin with a water depth of 1366 m.

The final array consists of 27 independent clusters, which are all connected to shore individually, as shown in Figure 2.3 on the left. The distance between the center of neighboring clusters is ∼300 m. Each cluster has eight strings, placed in a heptagon on a radius of 60 m from the central string, illustrated in the middle of Figure 2.3. All Optical Modules (OMs) are facing downwards and are mounted at the string over a difference of 540 m from 750 m to 1275 m in depth. Therefore one cluster is instrumenting approximately 40 Mt or $4 \cdot 10^{-2}$ km^3. On each string, 36 OMs with a vertical spacing of 15 m are divided into three sections with 12 OMs. This design leads to a total number of 288 OMs per cluster and 7776 OMs for the final stage of 27 clusters. The basic design of the OMs is explained in subsection 2.2.1.

In the middle of every section, a Central Section Module is placed, which digitalizes the signal, creates the trigger for the whole cluster and in case sends the data over the network. The network is a local-area-network (LAN) out of three levels and provides the readout and control of the detector.

Figure 2.4: *The Optical Module in GVD has a 10-inch PMT (golden), which is mounted inside a 17-inch pressure-resistant glass sphere. Between the glass sphere and the PMT an optical gel avoids total internal reflection. Therefore, the PMT appears so big on the photo. All electronic components inside the OM are attached to the base of the PMT. In subsection 2.2.1, the OM is explained in more detail. This photo was taken by F. Henningsen during the deployment in March 2017.*

These levels are the connections between the on-shore data processing center, the Cluster Center Modules, the Communication Module of every string and the Central Section Modules. The Central Section Module and the Network are explained in more details in subsection 2.2.2 and subsection 2.2.3, respectively.

Besides, every string has acoustic modules which are mounted over, under and inside the OMs sections. As sound waves in water have a very high attenuation length, the acoustic modules are used to calibrate the positions of the strings.

About 100 m under the last OM the strings are anchored to the sediment with weight. At the other end of the string are several floats approximately 20 m under the surface of the lake. This separation should mainly decouple the strings form the weather and current conditions on the surface. Furthermore, it allows divers to attach lifting gear without any need of a Remote-Operating-Vehicle (ROV).

2.2.1 Optical Module

One of the most important modules of every neutrino telescope based on Cherenkov light detection is the Optical Module (OM). As a light sensor, one Hamamatsu R7081-100 photomultiplier tube with a 10-inch (254 mm) hemispherical photocathode and quantum efficiency up to 35 % is used per OM. The PMT is mounted in a 17-inch (432 mm) pressure-resistant glass sphere with an optical gel. The
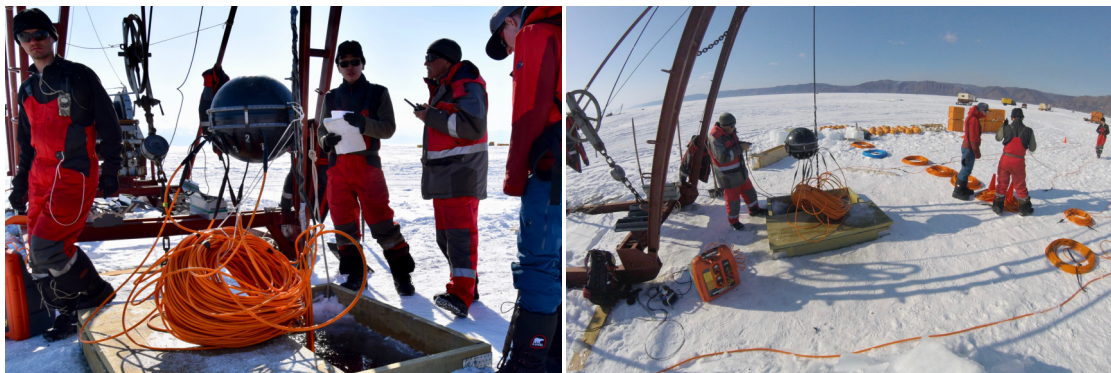
Figure 2.5: *During the deployment, cables for 6 OMs (half a section) have to be connected to the Central Section Module (black sphere in both pictures). For a more easy logic in the FPGA, all OMs are connected with 90 m cables, even if the OM is just 15 m away. Therefore a lot of cable has to be stored somewhere, e.g. close to the Central Section Module. Left picture taken by F. Henningsen.*

gel fills the gap between the glass sphere and the glass of the PMT. A high reflective index of the gel n_{Gel}, with $n_{Gel} \approx n_{Glass}$ suppress the reflexion R. This reduction be shown by the Fresnel equations, which simplifies for the normal incidence $\alpha = \beta = 0$ to

$$R = \left| \frac{n_{Gel} - n_{Glass}}{n_{Gel} + n_{Glass}} \right|^2 \approx 0 \tag{2.1}$$

for $n_{Gel} \approx n_{Glass}$. Also the angular acceptance for the PMT is extended by preventing total internal reflection at the boundaries.

Besides, the OM hosts some electronic components. The main parts are a high voltage power supply for the PMT, a two-channel preamplifier, two calibrated LED-flasher with about 479 nm and an OM controller board with a micro-controller. All these electric components are directly mounted to the PMT base. Around the equator where both glass hemispheres come together, a metal mount is the mechanical link to the string. A 5-pin SubConn connector is as the penetrator for the data cable, which transmits the communication to the micro-controller, 12 V DC and the preamplified analog PMT signal.

2.2.2 Central Section Module

All OMsare connected through a 90 m long cable to the central section module. This module has the same pressure housing as the OMs, but the glass is covered inside and outside by a black surface, preventing light emitted by the electronics to leave the casing.

Its main task is to digitalize the analog signal from all 12 connected OMs of this section at one 12 channel ADC-board. The ADC has a resolution of 12 bit and a sampling frequency of 200 MHz. An FPGA controls and processes the data from the ADC. The data is double buffered in one RAM block of 18 kB per block per channel. Therefore the signal is stored over an interval of 30 µs.
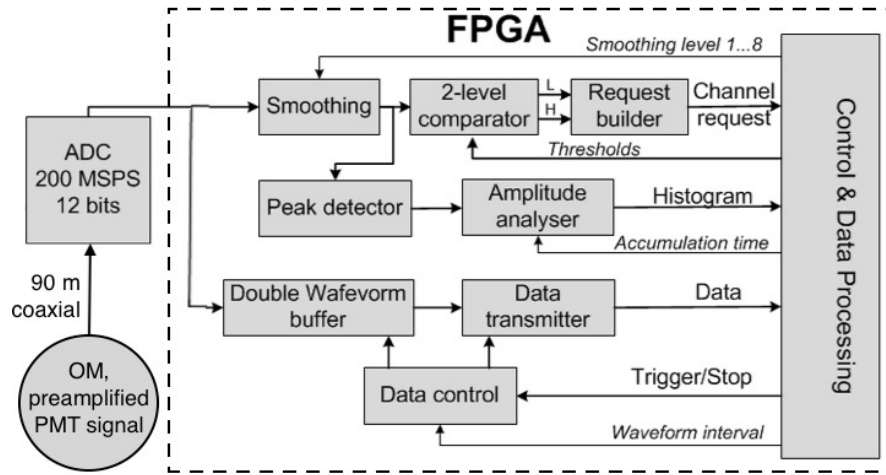
Figure 2.6: *This functional diagram of the FPGA (dashed part) logic shows the processing of the data of one OM (bottom left) in GVD. A buffer stores the data stream from the ADC (left) over an interval of 30 μs. When the signal (Trigger/Stop) for a cluster read-out arrives, the related data of 5 μs is transmitted. The basis of a cluster trigger is the 2-level-comparator with two defined thresholds. When the signal is over a threshold on two neighboring channels (OMs), the FPGA sends a read-out request to the Cluster Center. The schematic is from [5] and has been modified.*

The trigger is based on a 2-level comparator which compares two adjustable voltages against the signal. When the lowpass-filtered signal is over one of the adjustable voltages, the dependent output of the comparator will trigger. In normal operating mode, the two levels are set to 1.5 p.e. and 4.5 p.e. for trigger level L and H, respectively. In the FPGA an embedded hardware-software Coincidence Matrix with 12Hx12L is used to process the trigger. Another feature of the FPGA is a real-time data processing, which allows the filtering of the signal to compress the sent data by a factor of 10^{-2}. Therefore only those parts are sent where an excess over the threshold is observed. A block diagram of the FPGA is illustrated in Figure 2.6.

2.2.3 Detector Network

Every cluster has its connection to shore and therefore its own network and power supply. A sketch of the network is shown in Figure 2.7. The network of the cluster is a local-area network (LAN) with three levels. The first level is the ∼6 km connection from the on-shore data processing center to the Cluster Center Modules. With a speed of 1 Gbit/s it is well enough for the calculated data flow of 100 Mbit/s from the cluster. However, if necessary an update to at least 10 Gbit/s could be done with the existing hardware.

The second level is the connection of the Cluster Center Module to the Communication Modules of the strings with a length of ∼1 km. There some twisted-pair cables are used in combination with DSL technologies. This configuration gives a speed of up to 10 Mbit/s. The third level is the connection
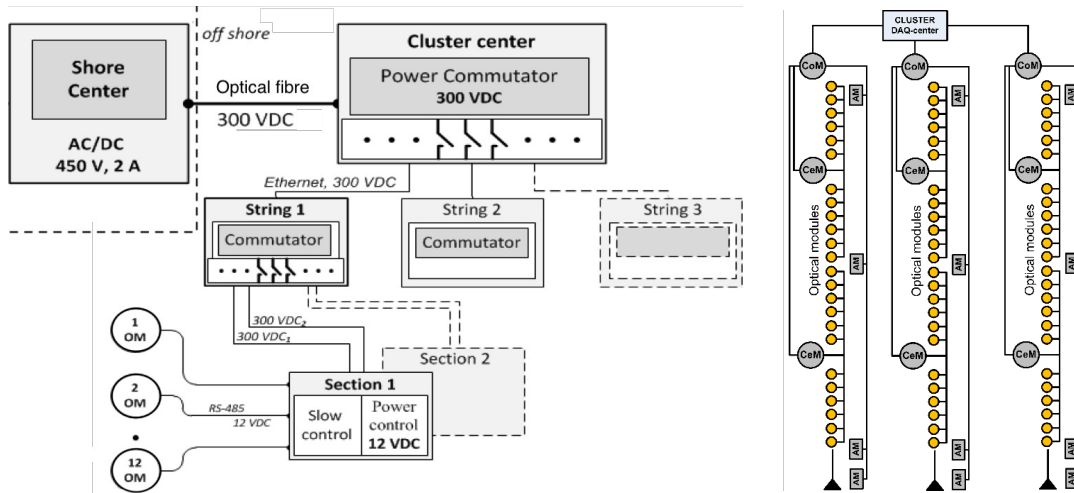
Figure 2.7: *Schematics of the GVD network for a cluster with shore connection (left) and one cluster (right). For a better overview only two sections per strings are illustrated. The schematics are from [3, 4] and have been modified.*

of the Communication Module of a string to the Central Section Module with up to $\sim$300 m.

All three levels use 300 V DC for the power supply. Only inside the Central Section Module a DC/DC-converter reduces the voltage to 12 V for the single OMs.

2.3 Trigger

In GVD a trigger and read-out are performed only among a single cluster, due to the separated connection to shore. With a connection length of $\approx$14 km for two Central Section Modules in two different clusters, the signal would need $\sim$60 μs. This duration is too long for the used buffer. However, if one event triggers two or more clusters, an offline analysis has to match the events inside the different datasets of the clusters.

The trigger is generated inside the FPGA of the Central Section Module by processing the L and H signal from the comparator. The primary operating mode is called *L & H trigger*, and it happens whenever a coincidence of at least one L and H is detected, in any adjacent optical modules of one section. Once recognized, the Central Section Module sends a request to the cluster center. There the read-out signal for the whole cluster is generated, and it is sent to all Central Section Modules. This process takes $\sim$15 μs from the first L and H signal.

If a Central Section Module receives the signal for the cluster-wide trigger, first the ADC buffering is stopped. Afterward, the read-out of the buffer is started, where the corresponding time interval of 5 μs is selected and transmitted to the data center on-shore.

With the L and H thresholds of 1.5 p.e. and 4.5 p.e., one cluster has a trigger rate of $\sim$100 MHz.
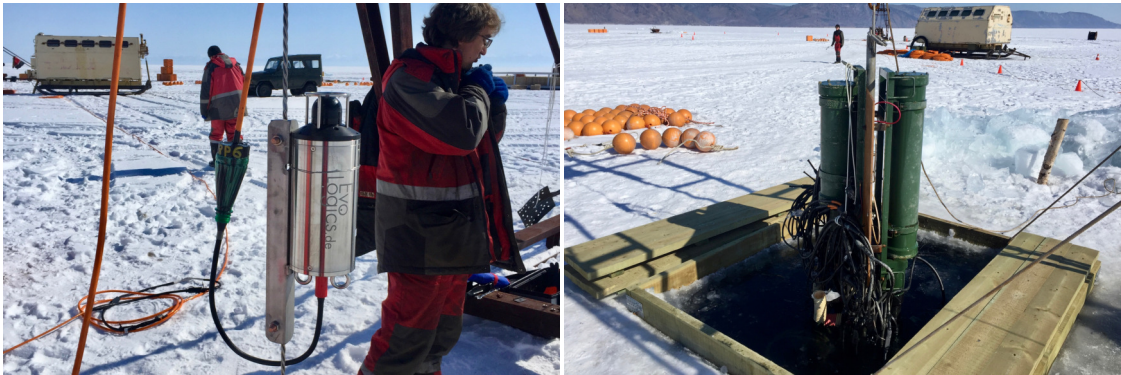
Figure 2.8: *Four acoustic modules (left picture) are placed at one string for the geometry calibration. The cluster center module (right picture) distributes and controls the network connection as well as the power supply for the cluster. It is also responsible for sharing the read-out signal (trigger) among the cluster.*

Figure 2.9: *The shore station is a former station of the Trans-Siberian Railway. On the left side of the station the new data acquisition center (white container) is placed.*

3 Precision Optical Calibration Module

The Precision Optical Calibration Module (POCAM) was initially designed as a new calibration module for the upgrade of the IceCube Neutrino Telescope [11]. The idea is to develop a device which can improve the calibration in IceCube-Gen2.

In 2014 the development started, and in early 2017 the first fully functional prototype was built for GVD (see chapter 2). This prototype functioned for the entire year in which it was deployed in Lake Baikal at a depth of 1000 m and temperatures down to −20 °C during the deployment. Just one year later,

three upgraded modules have been deployed in the *Strings for Absorption length in Water* (STRAW) successfully at a depth of 2600 m in the Pacific Ocean.

In this chapter, first, the significant uncertainties and the existing calibration methods of IceCube will be outlined (section 3.1). Followed by the motivation, concept, and development as well as the design of the POCAM in section 3.2. Finally, the essential parts of the POCAM will be explained in more detail.
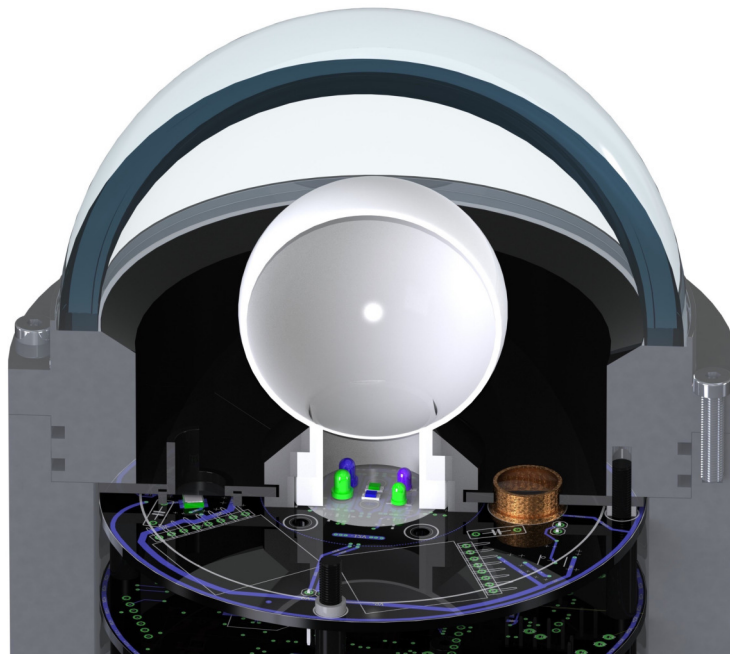
Figure 3.1: *Cutaway drawing of one hemisphere of the POCAM. The LEDs illuminate the integrating sphere from the bottom through the sphere plug. An Exploded-view drawing of this part is pictured in Figure 3.7.*
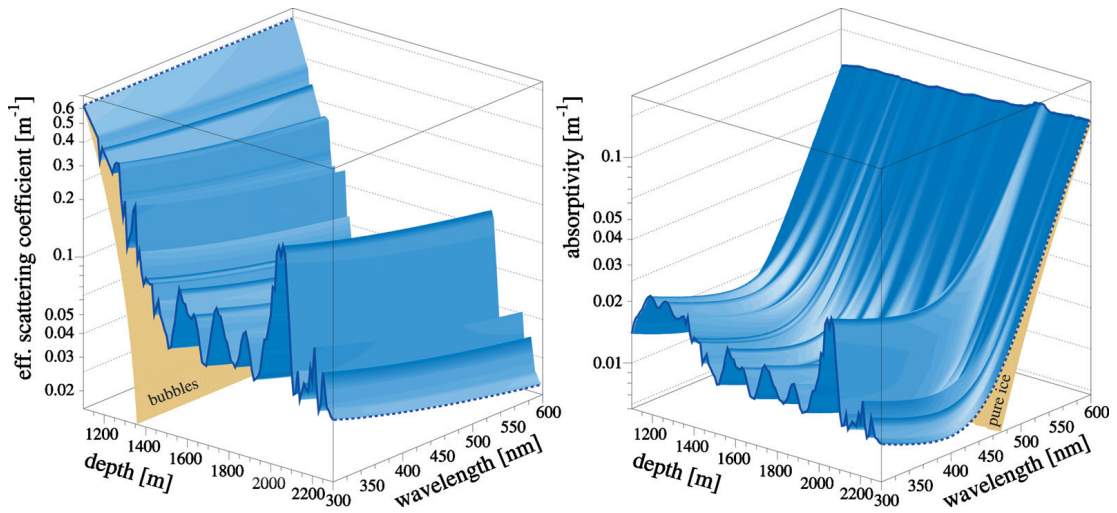
Figure 3.2: *The scattering-length (left) and absorption-length (right) in the ice as a function of depth and wavelength [1].*

3.1 Uncertainties in IceCube

For the motivation of the POCAM, it is essential to understand the uncertainties in IceCube and the existing calibration methods. Therefore, this section explains the uncertainties in the ice of the detector. Followed by a summary of other important uncertainties and the existing calibration methods.

3.1.1 Uncertainties of the Ice

One of the main uncertainties in IceCube is the optical properties of the Antarctic ice. The ice has grown over thousands of years and conserved particles from the historical climate conditions and global events like volcano eruptions or impacts of meteoroids.

The result is a horizontal layered structure with local differences in the optical properties. Besides, the ice of the drilled holes has a non-negligible amount of air bubbles due to the refreezing process. These bubbles are not uniformly distributed inside the hole, and they scatter light effectively. Both effects lead to strong local differences in the optical properties.

Like shown in Figure 3.2, scattering is dominant in comparison to absorption for Cherenkov light even in the purest ice. Therefore, a detected photon is most likely scattered one or multiple times between the emission and the detection. As scattering has an impact on the traveled distance of the detected photons, it also influences timing and intensity. Another effect comes with the air bubbles in
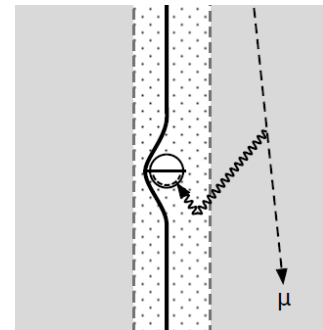
Figure 3.3: *The scattering of light at the air bubbles in hole ice [12].*

the hole ice, see Figure 3.3. Due to the refreezing process, the highest density is along the center of the hole ice at the position of the Digital Optical Modules (DOMs). Also, this has a significant influence on the angular acceptance of every DOM [12].

3.1.2 Other Uncertainties

Beside the ice properties also mechanical and electric characteristics have to be calibrated separately for every DOM. The precise positions and orientations of the steel rope, the data cable, and the DOMs have to be determined in the ice. In IceCube, this has been measured within 1 m precision. Steel rope and data cable create a shadow at a particular direction. The precise position of the DOM inside the detector is essential for the timing. The orientation has to be known for the DOM angular acceptance which is mainly a characteristic of the PMT. In IceCube, the azimuthal orientations of the DOMs are measured within 10° [12].

Every PMT with its read-out electronic has a different noise, gain, transit time and quantum efficiency. In IceCube, the DOM efficiency is known to within 10 %.

Some of this effects are more important than others, and some have been calibrated before the deployment. However, the event reconstruction needs good calibration strategies to minimize the uncertainties from all these effects. Otherwise, the uncertainties lead to significant errors in the energy and direction reconstruction, reducing the sensitivity to sources of astrophysical neutrino as well as the decreasing the precision of neutrino oscillation measurements. However, it can also prevent separation of rare tau-neutrinos ν_τ events from ν_e events, with its shape of a double or single bang, respectively. As the double bang will be separated just by some meters, it is therefore very similar to the single bang in the detector signal. A more detailed explanation of the errors and methods can be found in [12].

3.1.3 Existing Calibration Methods

In IceCube, the existing calibration methods use minimum ionizing muons, LED-flasher in every DOM and in-ice calibration lasers. Since a minimum ionizing muon loses a nearly constant energy per length, it can be used for the energy calibration and therefore to determine the angular acceptance and the DOM quantum effectivity. Therefore the muon path has to be calculated from the timing and DOM position. However, this reconstruction is also the most significant uncertainty of this method.

In total there are 12 LEDs inside every DOM separated into two groups. One is pointing horizontally outward, and the other is pointing upwards at an angle fo 45°. The LEDs can be flashed separately with a minimum pulse length of 7 ns and a beam width of 10°. Most of the LEDs have a wavelength of 405 nm. Based on LED flasher runs, the SPICE Mie model has been created as the default model for the optical properties of the bulk ice. Also, the more resent SPICE Lea has a similar basis and additionally includes azimuthal anisotropy in scattering. Moreover, the LED flasher can also be used for calibrating the hole ice, the DOM sensitivity as well as the detector geometry with DOM orientation and timing.
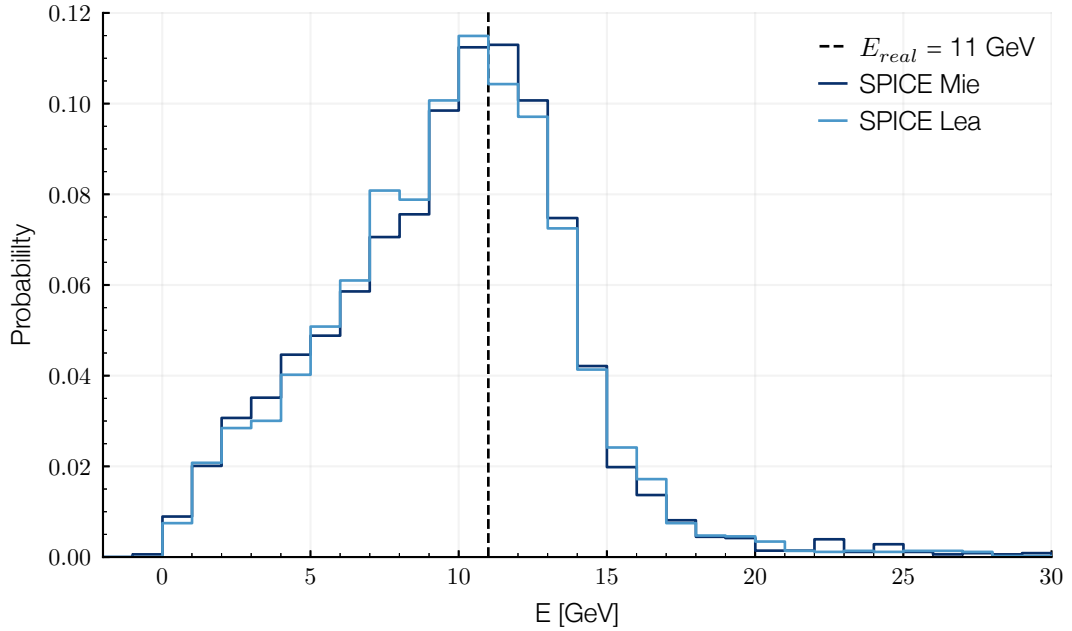
Figure 3.4: *Uncertainties in the energy reconstruction of electron neutrinos with 11 GeV in PINGU (charged current only). Here the probability function of the energy reconstruction is plotted for the two existing ice models, SPICE Mie and the more recent SPICE Lea. Since both ice models have a wide spread in the energy reconstruction, as shown in this plot, a better calibration is needed to minimize uncertainties in the reconstruction. Data taken from [12].*

In IceCube, the LED flashers showed the capability for calibration, but at the same time, the uncertainties of the flashers are the limits for further gains in calibration. The light output is not precisely known, because LEDs can undergo an emission loss of some percent over a decade. Furthermore, the orientation of the LEDs inside the DOM is only known to within 5 %. Together this can result in significant uncertainties as shown in Figure 3.4. For the next detector-upgrade, the flasher is planned to be optimized, and optical sensors should guarantee an in-situ calibration [12].

3.2 Concept of the POCAM

Like explained in section 3.1, IceCube needs good calibration strategies to minimize the uncertainties of the ice and the deployed modules. The concept of the Precision Optical Calibration Module (POCAM) is to optimize the light output for a robust and high efficient calibration method. The features are nano-second-pulsed light, isotropic emission, adjustable brightness, and different wavelength as well as in-situ calibration. In this section, the motivation of the POCAM features, the development and the concept of the essential parts are outlined.
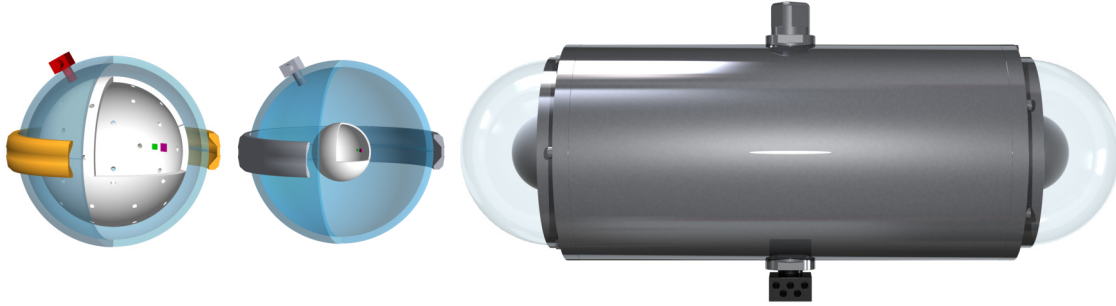
Figure 3.5: *Development of the POCAM. It started from a integrating sphere (left) with multiple ports, where the LED (purple) and the sensor (green) are placed inside the sphere. The simulation includes a harnest or waste-band (orange) for attaching the module to the line and a penetrator (red) for electric connections. The second iteration (middle) is a integrating sphere out of a semitransparent material with improved isotropy and timing. The final design (right) has two integrating spheres and the Electronic for flashing the LEDs and for the readout of the sensor is placed inside the middle part out of titanium. On the bottom there is the electric connector and at the top the vacuum port.*

3.2.1 Motivation for the Features

One of the most important features is the isotopic emission in 4π because this is comparable to the shower-like events the detector is measuring. This characteristic allows a more easy comparison of the detected signals from physic events with POCAM data than with LED flashers. Furthermore, isotropy makes the precise orientation of the POCAM less critical, as a perfect isotropic radiator projects the same intensity to all directions.

With the adjustable brightness, scans for different distances and energies can be performed to obtain, e.g., the absorption length, PMT efficiency or angular acceptance. Here should be mentioned, that for the calibration analysis the single photon detection at a DOM can be desirable. In combination with a different wavelength, also the wavelength dependency of the ice and modules can be studied. As mentioned in subsection 3.1.3, the in-situ calibration with pulse monitoring is crucial to detectors made for extended operating time, especially when the deployment or recovery of modules is very expensive or even impossible (recovery in IceCube). LEDs can undergo an aging process where they can lose several percents of their intensity. Therefore we have implemented a system to measure and monitor the light-output directly in the module.

The nano-second-pulsed light is important for timing and scattering measurements. In general, precision in timing is a function of the steepness of a rising or falling signal edge. A linear function can approximate the edge of a signal S

$$S(t) = mt \qquad \text{with } m = \frac{S_{max}}{t_{max}} \tag{3.1}$$

where the steepness m is defined by the pulse hight S_{max} and the time t_{max} after which S_{max} is reached. The steeper m is, the more precise the timing is defined, e.g the time when a threshold S_T

23

is reached.

$$t_T = \frac{S_T}{m} \tag{3.2}$$

$$\sigma(t_T) \sim \frac{\sigma(m)}{m^2} \tag{3.3}$$

This dependency lowers uncertainties in all time-related measurements, e.g., distance, geometry and the speed of light. The determination of the scattering can benefit as well as scattering can be derived by the change in steepness between the rising edge of the emitted and received signal. As scattered light has to propagate over a longer distance than direct light, the maximum of the pulse will be shifted by Δt. However, there is always light which is less scattered than the average and not scattered photons are also possible. These photons are delayed by less than Δt or even not delayed. Therefore, the detected pulse (S',t'_{max},m') starts with photons not delayed and the peak is shifted by Δt, as it is the sum of all measured photons. The steepness of both normalized signals $S = S' = 1$ is,

$$m = \frac{S}{t_{max}} = \frac{1}{t_{max}} \tag{3.4}$$

$$m' = \frac{S'}{t'_{max}} = \frac{1}{t_{max} + \Delta t} \tag{3.5}$$

With the difference in steepness is

$$\Delta m = m - m' = m \left(1 - \frac{1}{1 + \Delta t \, m} \right) \tag{3.6}$$

Consequently, a bigger m (steeper) result in a bigger Δm, which can be measured with lower uncertainties. This shows that the scattering calculation profits from a short pulse with a steep rising edge.

pulse

3.2.2 Development

One of the biggest challenges in the POCAM development has been, to achieve a 4π isotropy. In 2014, therefore, we had developed a GEANT4 simulation to investigate different designs effectively. The initial idea was to use a modified integrating sphere (also known as an Ulbricht sphere) about 120 mm in diameter with multiple holes. The light source and the light sensors were installed inside. A 17-inch glass housing similar to the DOMs should hosts all these parts. Optimizations of this design end up in a smaller to a smaller integration sphere from 20 mm to 50 mm out of a semitransparent material.

Both designs had the problem that the penetrator for electric connections and the waste-band for attaching the module to the line created much shadow. Besides the electric for flashing the LED and to readout the sensors was not even included. In late 2016, *F. Henningsen*, at this time a master-student of the group, came up with the idea to combine two integrating spheres for a 4π isotropy [17]. The pressure housing was changed to two glass hemispheres connected by a titanium cylinder.

With this approach, there was enough place to build in the electronic plus sensors. The images of this three iterations are shown in Figure 3.5.

3.2.3 Components

A cutaway drawing of the final POCAM for GVD is illustrated in Figure 3.6. The pressure housing has two glass hemispheres with a diameter of 7 inch (177.8 mm) and a thickness of 7 mm connected by a titanium cylinder with a diameter of 130 mm and a thickness of 15 mm. In total the length of the whole module is around 400 mm and it can handle a pressure of up to 1500 bar. A vacuum port and a 5-pin cable connector penetrate the titanium cylinder. The vacuum port is used to dehumidify the interior, and the 5-pin cable connector provides the connection to the detector with power supply and serial-communication.

Inside the POCAM there are five PCBs, one for the power supply and two sets of one analog and one digital board. This modular approach allows working with one hemisphere even when the other one fails.

The digital board hosts a μ-controller for the slow control and network communication. An FPGA controls the 10 MHz ADC, triggers 4 LEDs driven by a Kapustinsky flasher circuit and controls 2 FPGA driven LEDs. Where the Kapustinsky flashers allow only a fixed pulse-length and intensity, the FPGA flasher can be set up for a pulse-length of 10 ns to 80 ns, which also influences the intensity. To synchronize the flashing of both hemispheres a direct communication between the two FPGAs is

Figure 3.6: *Cutaway drawing of the full POCAM for GVD. Both hemispheres have a set of one analog (with the mounted integrating sphere), and digital PCBs and the fifths provides the power supply. Each side has 6 LEDs (upper center), a SiPM (left of LEDs), a Pin-Diode (right of LEDs) and amplifiers. The digital part provides, the trigger and DAQ as well as the communication with a μ-controller and FPGA.*

Table 3.1: *The used LEDs in the POCAM for GVD with their ID and the flashing circuit. The two digits of the LED-ID represent the corresponding bit (0x01≡000 001 bit register,..., 0x20≡100 000 bit register) in the register of the FPGA. For the communication to the POCAM the HEX-value is used.*

LED-ID	ID hex	Model	Wavelength [nm]	Color	LED driver type
L1	0x01	LZ1-60B200	455	blue	Kapustinsky
L2	0x02	ALMD-CB3D-Y1002	525	green	Kapustinsky
L3	0x04	ALMD-CB3D-SU002	470	blue	Kapustinsky
L4	0x08	XPEBGR-L1-...-00F01	525	green	Kapustinsky
L6	0x10	ALMD-CB3D-Y1002	525	green	FPGA
L5	0x20	ALMD-CB3D-SU002	470	blue	FPGA

included. This way, both hemispheres can flash simultaneously or separately, with any combination of flashing LEDs, e.g., only L1, L1+L2, all LEDs (see Table 3.1).

On the analog board, there are 6 LEDs and 4 Kapustinsky flasher circuits as well as a SiPM and Pin-Diode with amplifiers. The 6 LEDs are located in the center of the PCB, covered by the integrating sphere. The SiPM and the Pin-Diode are connected to two charge integrating amplifiers, the CREMAT CR-113 with 1.3 mV/pC and CREMAT CR-110 with 1.4 V/pC, respectively. Besides, on this board two DC-DC converters are located, to provide the two negative voltages of −12 V for the Kapustinsky circuits and −9 V for the CREMATs and two OpAmps.

3.3 Integrating Sphere

The integrating sphere is responsible for providing an isotropic light emission in 4π (all directions). In this section, the design and the emission profile of the integrating sphere are summarized.

3.3.1 Design

The isotropy is created by multiple diffuse reflections on the internal surface of the sphere, before the light leaves the semitransparent sphere. In a simplified picture without any losses like absorption or transmission through the surface, an integrating sphere will distribute a non-isotropic light pulse to an equal
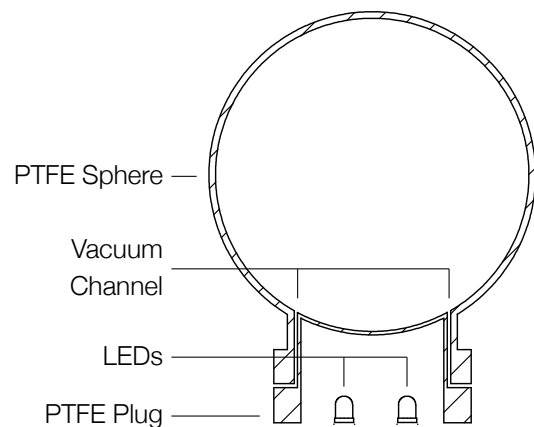
Figure 3.8: *Cutaway drawing of the integrating sphere with LEDs.*
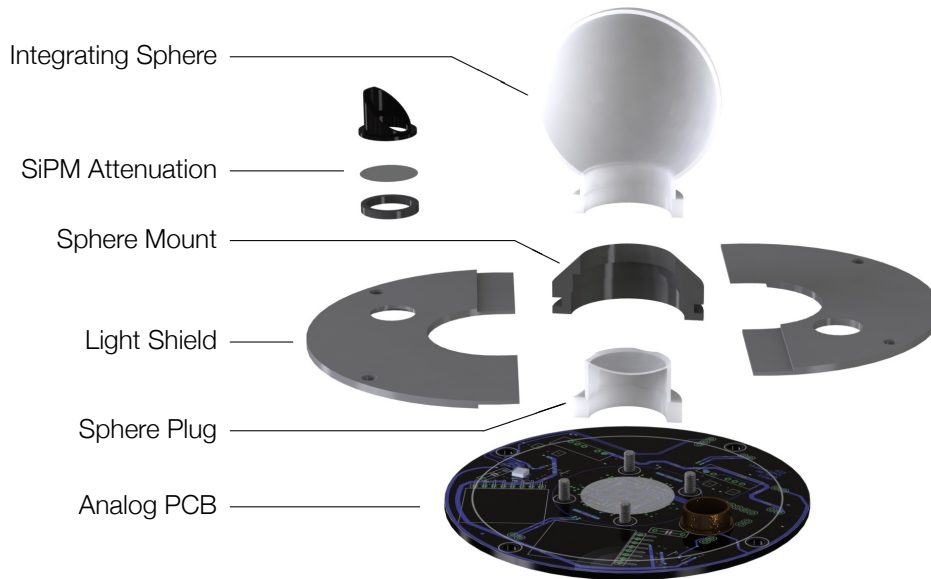
Figure 3.7: *Exploded-view drawing of the light emitting part of the POCAM. The SiPM (upper left on the Analog PCB) and the Photo-Diode (lower right on the Analog PCB) are used for in-situ calibration. A description of the integrating sphere and the Analog PCB can be found in section 3.3 and section 3.4, respectively.*

intensity on the whole internal surface after the time of several reflections [17]. Since the light should be emitted, the transmission can not be 0 and as every material is absorbing light, both parameters have to be optimized for the chosen material.

After some investigation, we selected polytetrafluoroethylene (PTFE) which is a commonly used diffusor. It is diffuse reflecting, the absorption is low, and the transparency can be set up with the thickness of the layer. Simulations in GEANT4, result in a sphere with a transmission of ∼5 %. However, measurements showed a transmission of ∼20 % at a thickness of ∼1 mm, which is also the limit for the machining of the *soft* PTFE. Hence, the challenge was to machine a sphere with a uniform thickness of ∼1 mm. Since machining a sphere without a hole is not possible, the design ended up in a sphere out of two parts. The main part is a nearly complete sphere with a mounting structure, and a plug finalizes the inner sphere. The Central-Workshop of the TUM physic department Both parts have been machined by the Central-Workshop of the TUM physic department with a CNC Lathe. Finally, a mounting structure out of glass-fiber reinforced plastic was created around the main part with a negative form. This way light emission from the non-spherical part is suppressed effectively by the black color of the plastic. The resulting design is pictured in Figure 3.1, Figure 3.7.

3.3.2 Isotropy of the Integrating Sphere

In an intensity scan, the integrating sphere has been measured for its isotropy. Therefore the integrating sphere was mounted on two rotating platforms, one responsible for the rotation in ϕ and
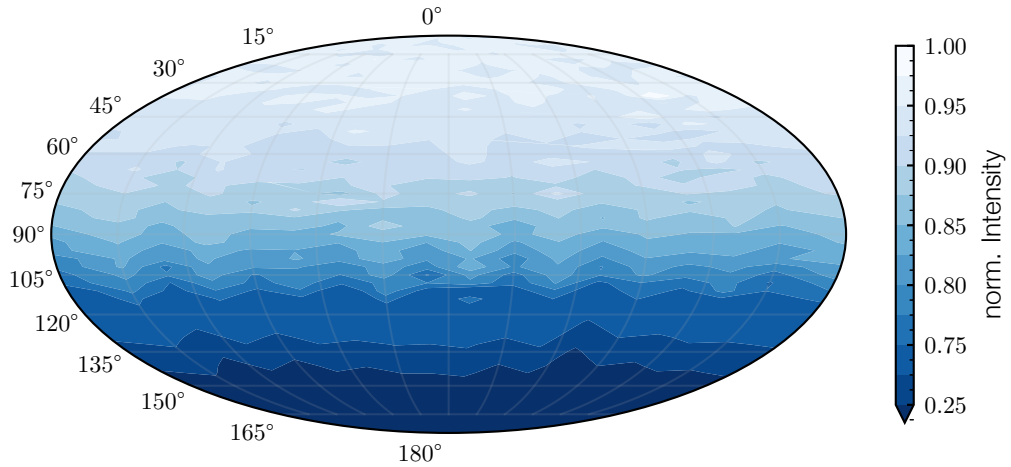
Figure 3.9: *Mollweide-Projection of the isotropy measurement of the integrating sphere. A Kapustin-sky circuit similar to POCAM illuminated the integrating sphere*
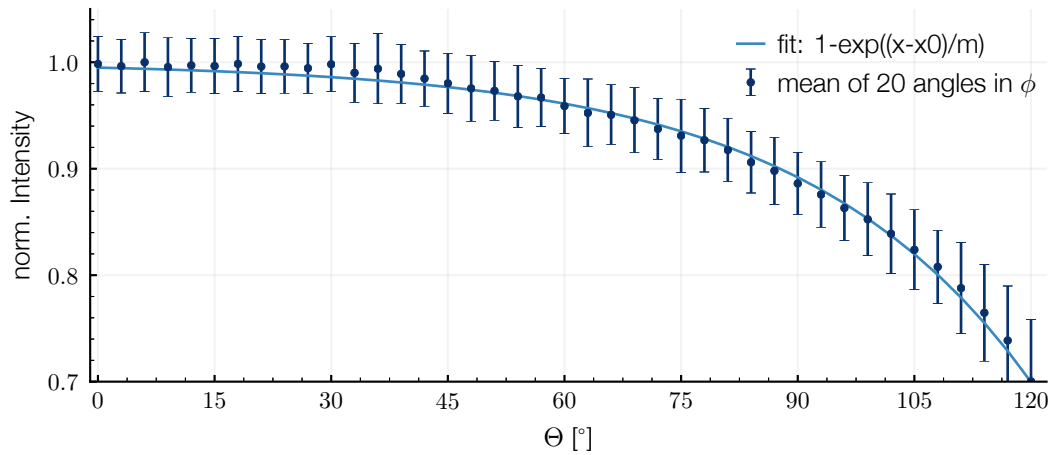
Figure 3.10: *Isotropy measurement of the integrating sphere. As variations in ϕ for a certain Θ are small, the average intensity in ϕ is plotted with standard deviation in ϕ. The profile can be fitted with an exponential function ($m = 29.3°$, $x_0 = 155.3°$) [17].*

the other in Θ. The scan was performed over an total of 918 pixel for 20 different angles in ϕ over 2π ($\Delta\phi =20°$) and 51 angles in Θ from 0° to 150° ($\Delta\Theta =3°$). The LED was flashed with the same Kapustinsky circuit which is also used in the POCAM.

As variations in ϕ for a certain Θ are small, the average intensity in ϕ over Θ with standard deviation in ϕ is plotted in Figure 3.10. In the range 0° < Θ < 30° the emission is nearly isotrop and at $\Theta = 90°$ is around 90 %. The whole profile can be fitted reasonable well with the function

$$I(\Theta) = 1 - e^{(x-x_0)/m} \tag{3.7}$$

and $m = 29.3°$ and $x_0 = 155.3°$. In addition this measurement was repeated with several different LEDs, to measure the dependency on narrow or wide emitting beams. But no relation could be found in the emitted profile and therefore, the influence of the emitting characteristic of the LED is negligible [17].

3.3.3 Isotropy of the POCAM

In the previous subsection 3.3.2 the angular emitting profile was shown for a single integrating sphere. In the POCAM the emission in 4π is created by a simultaneously flashing of two integrating spheres. Therefore, the intensity profile of the two spheres $I_I(\phi,\Theta)$ has to be combined, by taking into account the glass sphere with its titanium connector and the surrounding water. In this section an analytical approach is outlined to estimate the POCAM isotropy $I_P(\phi,\Theta)$ in 4π from the emission profile of a

Figure 3.11: *The path of the light in a simplified picture at $\Theta\sim90°$. The integrating sphere (dark blue) is projected through the glass hemisphere (light blue) into the surrounding water. The titanium housing (black) is creating a shadow, which effect is outlined in this section.*

single integrating sphere, with a scale function $S(\Theta) \in [0,1]$, $\forall\Theta$ and the formula for one hemisphere

$$I_P(\phi,\Theta) = I_I(\phi,\Theta)\, S(\phi,\Theta) \tag{3.8}$$

The integrating sphere can be assumed to have a point-source-like light emission. Intensity measurements for different distances of detector and integrating sphere indicates

$$\frac{I_{I1}(\phi,\Theta)}{r_1^2} = \frac{I_{I2}(\phi,\Theta)}{r_2^2} \qquad ;\forall\phi \in [0,2\pi], \Theta \in [0,\pi] \tag{3.9}$$

for I_i measured at r_i with $i \in 1,2$ [17]. Because of that, the emission of the sphere can be assumed to be parallel to the normal of the sphere surface. This feature simplifies the optics with the glass and water, as nearly both centers, of the integrating sphere and the glass sphere, match. Hence, there is no refraction at the transition from air to glass and further to water, as the incoming α and

outgoing β are both 0. That is why the intensity profile from the integrating sphere can be assumed to be similar if measured in water. This assumption does not hold in an absolute sense as absorption is happening at the edge of glass and water, but it should be a good approximation for the relative intensity.

As the glass of the housing is only covering 2π, the intensity for the other 2π is reduced. To describe this shadow, the intensity is assumed to be directly proportional to the visible area of the integrating sphere under the angle Θ. Therefore the angle has to be determined, where the shadow of the housing starts and where the light of the integrating sphere is completely blocked. With a radius $r_1 = 24\,\text{mm}$ of the integrating sphere and the inner radius of the glass $r_2 = 50.2\,\text{mm}$, the angels are

$$\tan(\alpha) = \frac{r_1}{r_2} \qquad\Longrightarrow\qquad \alpha \approx 25.6° \tag{3.10}$$

$$\sin(\beta) = \sin(\alpha)\frac{n_{air}}{n_W} \qquad\Longrightarrow\qquad \beta \approx 19.0° \quad (n_{air} = 1,\, n_W = 1.33) \tag{3.11}$$

Therefore, the boundary conditions of the scale function are $S(90° + \beta) = 0$ and $S(90° - \beta) = 1$. In the following, the scale function should be a description of the percentage of the visible area of the integrating sphere under the angel Θ.

$$S(\Theta) = S(\phi, \Theta) \tag{3.12}$$
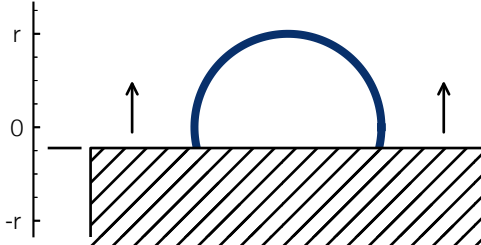
Figure 3.12: Appearance of the sphere at $\Theta \sim 90°$. The intensity of the integrating sphere (blue) at the angle Θ can be approximated with visible area of the integrating sphere. Therefore the area, covered by the titanium housing, has to be subtracted.

Without obstacle, the visible area of the integrating sphere is a circle with the outer radius of the integrating sphere. When the titanium is blocking the field of view, the visible area is reduced. This reduction can be described with a non-transparent rectangle moving over the circle like shown in Figure 3.12. Therefore, the cross-section of the rectangle and circle have to be subtracted off the area of the circle. From the equation of the radius $r = \sqrt{x^2 + y^2}$, the circle can be described, separated in two hemispheres, by the function

$$y(x) = \pm\sqrt{r^2 - x'^2} \qquad x \in [-r, r] \tag{3.13}$$

For simplification and as it does not interfere with the result, the radius is set to r = 1. By integrating the function from -1, the visible area $A(x)$ of the integrating sphere is

$$A(x) = 2\int_{-1}^{x} \partial x'\, y(x') = 2\int_{-1}^{x} \partial x' \sqrt{r^2 - x'^2} \qquad \text{with } r \in [-1, 1] \tag{3.14}$$

$$= x\sqrt{1 - x^2} + \arcsin(x)\Big|_{-1}^{x} \tag{3.15}$$

Now, x has to be -1 if $\Theta < 90 - \beta$, +1 if $\Theta > 90 + \beta$ and described by a linear function to result in a
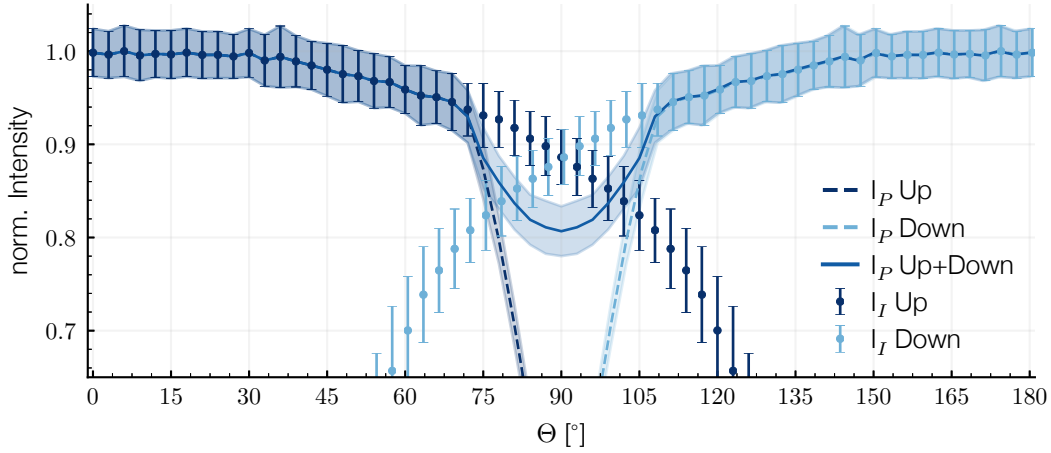
Figure 3.13: *Isotropy of the POCAM. For each hemispheres (up and down), the profiles for the integrating sphere I_I and the estimated POCAM emission I_P are plotted. In addition, the combined sum I_P of both hemispheres is illustrated. The derivation of I_P can be found in subsection 3.3.3 and here $\beta_0 = 2°$.*

continuous function.

$$
x(\Theta) = \begin{cases} -1 & \text{if } \Theta < 90 - \beta_0 - \beta \\ (\Theta - (90 - \beta_0))/\beta & \text{if } 90 - \beta_0 - \beta \leq \Theta \leq 90 - \beta_0 + \beta \\ +1 & \text{if } \Theta > 90 - \beta_0 + \beta \end{cases}
\tag{3.16}
$$

As the boundary of the glass is a bit lower than $\Theta = 90°$ due to the glue, β_0 is introduced as the thickness of the non-transparent area and which is in the range from 1° to 10°. Hence, the scale
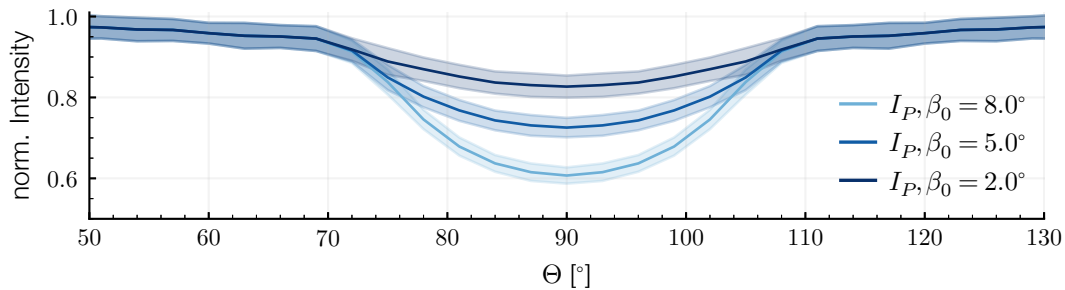
Figure 3.14: *Impact of a shadow created at the boundary of glass and titanium. The size of the shadow is characterized by β_0. Like shown in this plot, β_0 has to be minimized as much as possible.*

31
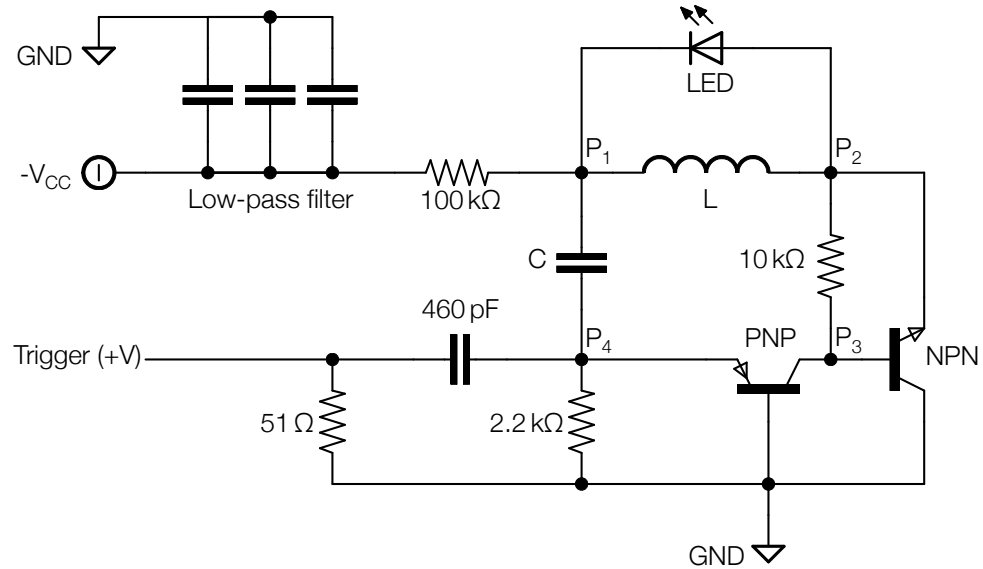
Flasher Circuit

Figure 3.15: *The Kapustinsky flasher circuit in the POCAM for a single LED. A trigger signal with a positive voltage, lead to a discharge of the negative charged capacitor C over the LED and the inductance L. To set up the intensity and length of the light pulse, a combination of LED, L and C has to be chosen and optimized.*

function is

$$S(\Theta) = \frac{1}{\pi} A(x(\Theta)) \tag{3.17}$$

normalized with the area of a circle with $r = 1$. Combining eq. (3.8) and eq. (3.14) as well as eq. (3.17) result in

$$I_P(\Theta) = I_I(\Theta) \frac{1}{\pi} A(x(\Theta)) \tag{3.18}$$

$$= I_I(\Theta) \frac{1}{\pi} \left(x(\Theta) \sqrt{1 - x(\Theta)^2} + \arcsin(x(\Theta)) + \frac{\pi}{2} \right) \tag{3.19}$$

with $x(\Theta)$ from eq. (3.16). Applied on the measured data (I_I), the result for $\beta_0 = 2°$ is plotted in Figure 3.13, together with I_I and I_P. To study the impact of β_0, the angular profile of the POCAM is illustrated for three different angles in Figure 3.14. For $\beta_0 = 2°$ relative intensity has a minimum of 85 %, but with $\beta_0 = 2°$ the minimum is already at 60 %. Therefore, β_0 or the used glue has to be minimized as much as possible at the boundary of glass and titanium housing. However, there are mechanical limits and the effect influences only the horizontal areas from 70° to 110°.

3.4 Flasher Circuit

The flasher circuit is responsible for guiding LEDs ns-pulse emission with a certain intensity. In the case of the POCAM for the GVD application, two types of flasher circuits are implemented. Four LEDs are flashed with a Kapustinsky circuit, and two are driven by FPGA controlled circuit. The
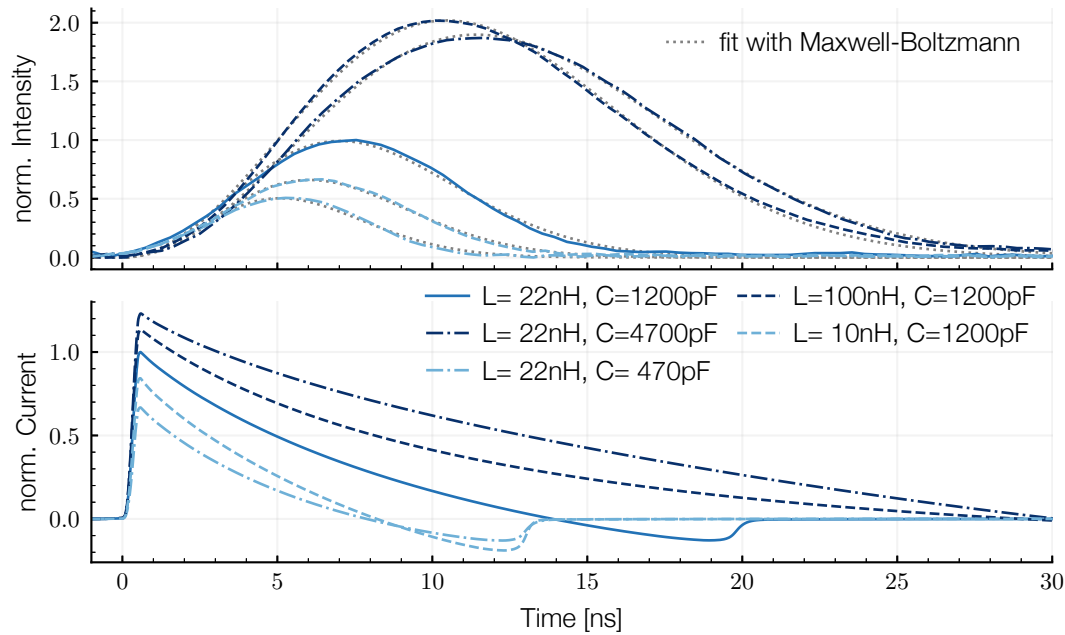
Figure 3.16: *Comparison of simulation and measured pulse of a LED flashed by a Kapustinsky circuit. As a simulation of the time-emission profile of a LED is complex, here the measured intensity (top) is compared with the simulated current through the LED for several configurations of L and C. The simulation can not predict the intensity well, because the integrated areas of current and intensity should be proportional. However, the timing or pulse length gives comparable results. Moreover, the measured intensity can be fitted with a Maxwell–Boltzmann distribution and the fit results are listed in Table 3.2. The measured data are from [17], and the simulation was performed with SPICE.*

Kapustinsky circuit is a reliable and straightforward LED driver, which is producing a stable ns-long pulse. The FPGA controlled circuit allows to set up the emission length from 10 ns to 80 ns by software. This gives the possibility to control the total emitted energy by the LED. For a long pulse length of more than 40 ns, the total emitted energy exceeds the brightest Kapustinsky driven LEDs. Therefore, the FPGA controlled circuit gives the chance to probe bigger distances to the OMs.

3.4.1   Concept of the Kapustinsky Circuit

In the following the Kapustinsky LED driver will be explained by referring to Figure 3.15. The basic idea behind the circuit is to discharge the capacitor C over the two transistors (NPN, PNP). Therefore, the capacitor C is charged with a negative voltage $-V_{CC} = -12$ V. To decouple noise from and to other components, e.g., another Kapustinskys, a low-pass filter and a resistor with 100 kΩ is placed between V_{CC} and the flasher circuit.

As long as no trigger signal is applied, the trigger and the connection point P_4 are grounded ($V_4 = 0$)

over the two resistors with $51\,\Omega$ and $2.2\,\mathrm{k}\Omega$, respectively. P_1, P_2 and P_3 (V_1, V_2, V_3) are at the level of $-V_{CC}$. Hence, the PNP resistor is closed, because there is no voltage difference V_{EB} between emitter-base (arrow-bottom at PNP) and base-collector V_{BC} has a negative potential difference. Also the NPN is closed, because $V_{EB} = V_{32} = V_3\text{-}V_2 = 0$ and $V_{BC} = V_3\text{-}V_{GND} = -V_{CC}$ ($V_{GND} = 0\,\mathrm{V}$).

For the following explanation of the process of the flashing, all connections through a resistor can be neglected, because of the high frequencies. If a positive trigger signal, e.g., square wave, is applied, the uncharged $460\,\mathrm{pF}$ capacitor let the signal pass and it will rise V_4 to a positive level. Now the positive potential difference V_{EB} at the PNP opens the transistor, which leads to $V_4{>}V_3{>}0\,\mathrm{V}$, and finally opens the NPN. Hence, the capacitor is connected to GND, and it is discharging over the inductance L and the LED, which lights up. After some nanoseconds, when $|V_{12}|$ is dropping, the inductance L is inducing a current, which is discharging the internal p–n junction of the LED. Without this discharge, the LED would decrease its intensity more slowly. As now the capacitor C is discharged and V_{12} is only oscillating a bit around $0\,\mathrm{V}$ because of the inductance L, there is no further light emission of the LED.

After some $100\,\mathrm{ns}$, the two resistors with $2.2\,\mathrm{k}\Omega$ and $10\,\mathrm{k}\Omega$ have lowered V_3 and V_4 till both transistors are closing again. Now C is charged over the $100\,\mathrm{k}\Omega$ resistor and the circuit is ready for a emission when C if fully charged after $t = RC$, which is $\sim 0.5\,\mathrm{ms}$ for common values of R and C.

3.4.2 Pulse Shape of the Kapustinsky Circuit

It is quite obvious that a bigger capacity C results in longer and brighter light emission. However, the same effect has also a bigger inductance, as it has a bigger internal resistance and will bypass more charge from the capacitor to the LED, which also results in long and brighter light emission. In an approximation both, the brightness and pulse length, are proportional to $1/\sqrt{LC}$, similar to an oscillating circuit. However, the capacity and resistance of the LED have also a big impact on both characteristics. Therefore the circuit was simulated in SPICE and compared to measurements like illustrated in Figure 3.16. The simulation gives comparable results for the pulse length, but it is not accurate for the emitted intensity. Hence, for every LED the inductance L and capacitor C has to be optimized for a given pulse shape. Typical light pulses are some nano-seconds long and emit 10^7 to 10^8 photons [17].

It turned out that the measured pulse can be fitted with a Maxwell–Boltzmann distribution

$$I(t) = At^2 e^{\dfrac{-mt^2}{2}} \tag{3.20}$$

and the resulting fit parameters are listed in Table 3.2 for the 5 configurations.

3.5 In-situ Calibration

Like explained in subsection 3.1.3 and section 3.2, the POCAM needs methods for an in-situ calibration. In the POCAM for GVD, two independent light sensors per hemisphere are used to monitor the

Table 3.2: *Resulting fit parameters for the measured pulses of 5 configurations fitted with a Maxwell–Boltzmann distribution. The fits and the data of the measurements are plotted in Figure 3.16.*

Configuration	C1	C2	C3	C4	C5
L [nH]	22	22	22	100	10
C [pF]	1200	4700	470	1200	1200
m [10^{-2}/ns^2]	4.064	1.535	7.718	1.826	5.509
A [10^{-2}/ns^2]	5.481	3.958	5.291	5.009	4.943
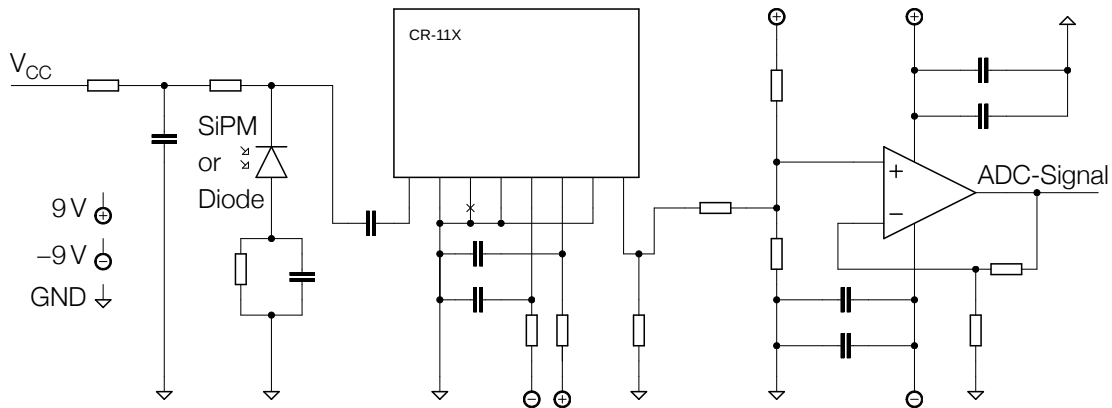
Figure 3.17: *Schematic of the SiPM and Pin-Diode amplification circuit. The nano second long signal of the SiPM or Pin-Diode is amplified a CREMAT (CR-11X), which is a charge integrating amplifier. The CREMAT outputs a signal in the order of some micro seconds, long enough to be measured with the 10 MHz ADC. Between the output of the CREMAT (right pin) and the signal for the ADC, a kind of summing OpAmp lifts the signal by 0.1 V. The SiPM bias-voltage (V_{CC}) is controlled by the μ-controller.*
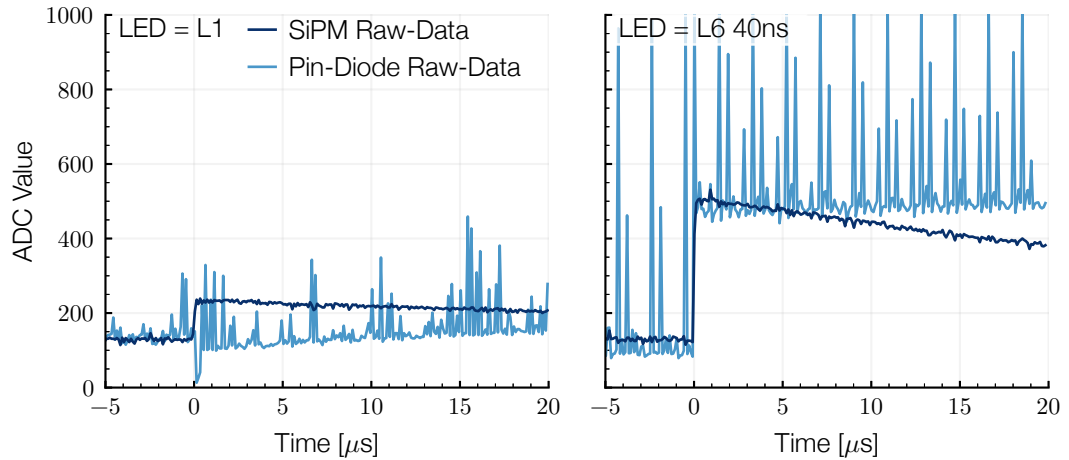
Figure 3.18: *Raw data of both light sensors for the in-situ calibration for two LEDs. Here, one randomly chosen event of L1 (left) and L6 (right) is plotted. The L6 is driven by the FPGA flasher, which allows to set up the pulse length, which is here 40 ns. As both sensors are connected to the SiPM bias voltage, only one sensor gives reasonable results, due to crosstalk on the PCB. Here, the bias voltage is over the breakdown voltage of the SiPM. That is the reason why only the SiPM provides useful data. However, for more intense pulses, e.g., L6 with 40 ns, this effect gets smaller. Therefore and to show a problem of the high amplification of the Cremat and crosstalk of the DCDC-converters with ∼2 MHz, the data of the Pin-Diode is also plotted.*

emitted light pulse. The two light sensors are a SiPM and a Pin-Diode. In this section, first readout and the sensor electronics are outlined, followed by an explanation of the raw data and the analysis. In the following, all plotted data are taken from runs in GVD.

3.5.1 Sensor Electronics and Readout

For simplification of the electronics, the readout of both sensors is done with a 10 MHz ADC. To measure the nanosecond long light emission, a charge integrating amplifier is placed between the sensor and ADC. Here, the Cremat CR-110 is used for the Pin-Diode and the Cremat CR-113 for the SiPM with a amplification of 1.4 V/pC and 1.3 mV/pC, respectively [14, 13]. To prevent a negative baseline, a kind of summing OpAmp circuit raises the signal to the ACD by 0.1 V. The bias-voltage for the SiPM is controlled by the μ-controller. This allows to measure the SiPM breakdown voltage in-situ and offers the possibility to set up the gain of the SiPM by software. The schematic is illustrated in Figure 3.17.

A disadvantage of this schematic is crosstalk of both sensors, as they share the same V_{CC}. As mentioned, the Pin-Diode gives only a weak signal, which has to be amplified with a high gain. To prevent crosstalk over V_{CC}, a low-pass-filter is included. However, the filter is not enough to prevent the disturbance by the strong signal of the SiPM. However, the Pin-Diode cannot cause any crosstalk
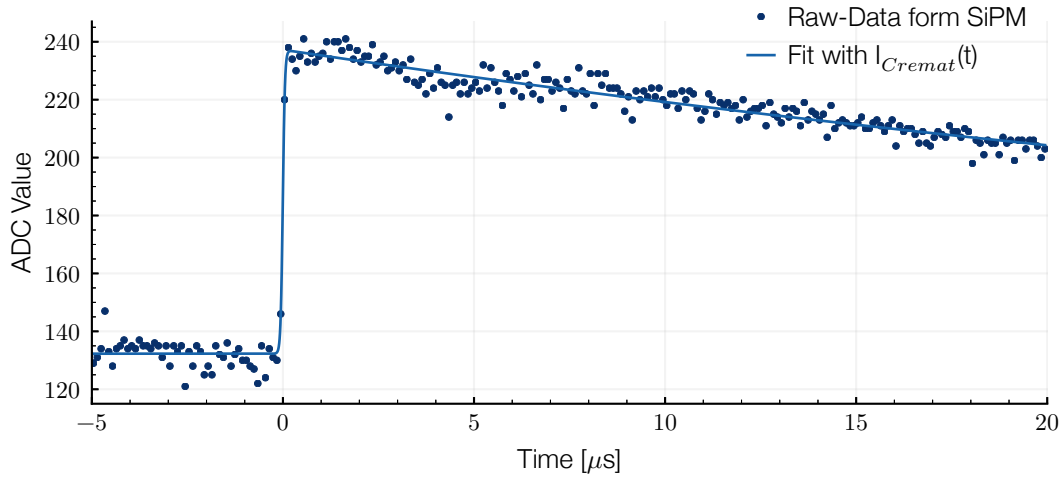
Figure 3.19: *Fit of the in-situ calibration data. The data of the SiPM for a random event of L1 are fitted with eq. (3.21). For a further analysis of the data, the hight of the step at t = 0 μs (in eq. (3.21) Δy) is the most important characteristic, as it is directly proportional to the total emitted energy.*

to the SiPM, due to the weakness of the signal. Therefore only one sensor provides reasonable results, and the sensor can be selected by the chosen V_{CC}. Is V_{CC} higher than the breakdown voltage of the SiPM, the SiPM is *switched on* and provides data like shown in Figure 3.18. If V_{CC} is lower than the breakdown voltage, the SiPM is *switched off* and therefore the Pin-Diode shows no crosstalk and can be used for the analysis.

Another problem is the noise in the data of the Pin-Diode. This problem is crosstalk of the two DC-DC-converters on the analog board, which provides the −12 V for the Kapustinsky circuit and 9/−9 V for the Cremats and the OpAmps. Both converters have an internal switching frequency of ∼2 MHz, resulting in an oscillating noise pattern, which is visible in Figure 3.18. This problem was already recognized during the design process of the PCB. Therefore the GND plane of the sensors from separated to the GND plane of the DCDC. Both are only connected at specific points, to prevent this crosstalk. However, the data can still be used for the analysis by filtering the overshoots, as less than 50 % of the data-points show the noise.

If the POCAM is flashing and the monitoring is switched on, the FPGA is reading the ADC values and sends it to the μ-controller, which saves it. Later, this data is downloaded over the serial connection. The software of the FPGA allows to set up the number of ADC samples, before it triggers a LED, in order to record the baseline properly. Here should be mentioned, that the FPGA is triggering the LED 5 clock cycles later than configured with the settings. This bug means, setting up 50 ADC samples for the baseline results in 55 ADC samples for the baseline.
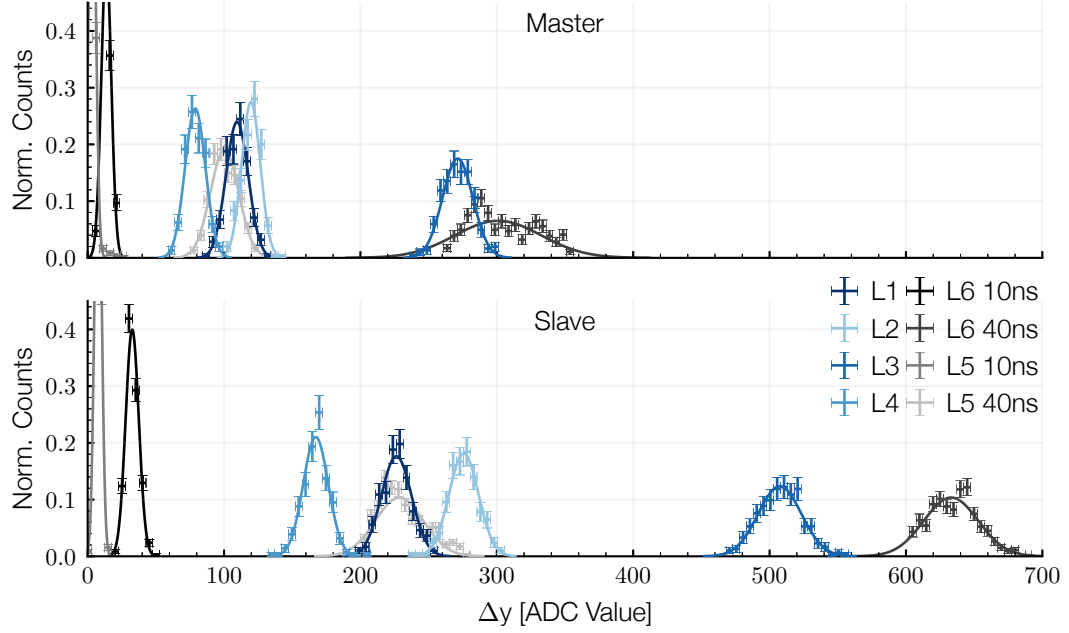
Figure 3.20: *Histogram of the fit parameter Δy for each LED and hemisphere. The underlying dataset of Δy comes from the fits of each event like shown in Figure 3.19. Besides, the data of each LED is fitted with a Gaussian distribution. The difference in the Δy of master and slave are uncertainties in the hardware and temperature differences, as the slave is placed on the upwards facing side. By assuming an equal intensity of each LED of both hemispheres and a similar integrating sphere, a linear fit from Figure 3.21 can correct this shift. The corrected fit values are summarized in Table 4.1.*

3.5.2 Data Analysis

In Figure 3.18 the data of both sensors is plotted for a randomly chosen event of L1 and L6 with 40 ns. The rise time of the Cremat is smaller than the ADC sampling rate, and the signal drops exponentially to the baseline in ∼500 µs or ∼150 µs for the CR-110 and CR-113, respectively. This signal shape can be fitted with a combination of tanh() and an exponential decay

$$I_{Cremat}(t) = \frac{\Delta y}{2}\left(\tanh\left(m_{tan}(t-t0)\right)+1\right)e^{\frac{-(t-t0)}{m_{exp}}} \tag{3.21}$$

where t_0 is the time of the rising slope, m_{tan} is its steepness, m_{exp} is the decay time and Δy is the hight of the signal. Δy is also the most relevant value, as it is directly proportional to the measured charge with the factor 1.4 V/pC and 1.3 mV/pC for the Pin-Diode and SiPM, respectively [14, 13]. Here should be mentioned, that a fit of this function is very unstable to the starting value of x_0, which is principally known because of the settings of the run. However, another way is to increase the data points synthetically by an interpolation. A fit of a random event of L1 is plotted in Figure 3.19.

In Figure 3.20, the fitted signal hight (Δy) of all LEDs is histogramised for both hemispheres, Master
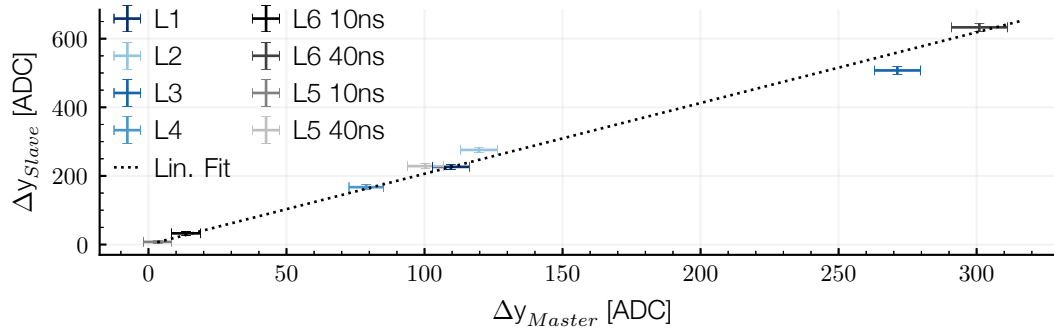
Figure 3.21: *Calibration curve to compare the in-situ calibration data of master and slave. Here the fit values from Figure 3.20 are visualized by plotting μ_{Slave} (or Δy_{Slave}) against μ_{Master} (or Δy_{Master}) for each LED. The result of the linear fit is used to correct the shift in the ADC readings between the two hemispheres in Table 4.1.*

and Slave. Besides, the FPGA driven L6 and L5 are plotted for two pulse lengths of 10 ns and 40 ns, to show the effect and range of the differences in the intensity. At the minimum pulse length of 10 ns, the pulse is faint for both L6 and L5, but at 40 ns both are at the level of the LEDs driven by the Kapustinsky circuit and 80 ns would exceed the ADC range of 1024 with the here used gain of the SiPM. In general, the green L6 has a higher intensity than the blue L5. The Kapustinski driven LEDs, show exactly the opposite, as the blue L1 and L3 are brighter than their green partners L4 and L2, respectively.

3.5.3 Sensor Calibration

The comparison of master and slave shows a shift of the absolute Δy values from the ADC. The reason for this shift is differences in the hardware and electrical components as well as a difference in the temperature of master and slave. These uncertainties are the integrating sphere, the LED itself, the attenuation foil which is mounted between integrating sphere and SiPM, the SiPM itself, the bias voltage of the SiPM, the Cremat, the OpAmp, and the ADC as well as the $-12\,\text{V}$ for the Kapustinsky flasher circuit. In principle, this effects should be corrected with data from calibrations in the lab, e.g., measuring the same standardized light pulse with master and slave for various temperatures of the board. Unfortunately, these measurements have not to be done, due to time constraints of developing and building this prototype for GVD.

In the following, the calibration technic should be shown with the data itself. Therefore, no major differences in both hemispheres concerning the LEDs and the integrating spheres have to be assumed. In the first order, all other uncertainties should result in a linear shift of Δy without any offset, which should be visible in the data. Therefore the histogramised distribution in Δy of each LED has to be fitted with a Gaussian function

$$y = A e^{\frac{x-\mu}{\sigma}^2} \tag{3.22}$$

39

In-situ Calibration

Table 3.3: *Summary of all six LEDs and their pulse intensity monitored by the SiPM. All data are from the SiPM of the POCAM during a run in GVD and downloaded over the serial connection. μ and σ are the mean and the standard deviation of the monitored intensity Δy. Here, the data of the slave was shifted with the correction function of Figure 3.21.*

LED-ID	Master Pulses	μ	σ	Slave Pulses	μ	σ
L1	502	109.5±0.4	7.7±0.2	729	110.0±0.4	5.0±0.3
L2	548	119.0±0.3	7.2±0.2	746	134.8±0.4	5.2±0.3
L3	519	270.9±0.6	12.0±0.4	755	247.7±0.6	7.4±0.4
L4	521	79.2±0.3	7.3±0.2	611	82.0±0.4	4.5±0.3
L5 10ns	431	3.0±0.2	3.2±0.1	564	3.7±0.1	1.3±0.1
L5 40ns	528	100.3±0.5	10.4±0.4	751	111.8±0.7	8.6±0.7
L6 10ns	482	13.6±0.2	3.7±0.1	711	16.0±0.2	2.4±0.1
L6 40ns	466	307.3±1.6	25.4±1.3	533	309.9±1.1	9.7±1.0

where y is the number of counts in a bin of the histogram, A is the amplitude of the function and μ together with σ are the characteristic Gaussian quantities for the position and width. μ is the mean of Δy with the error σ. The resulting fits are plotted in Figure 3.20. In Figure 3.21, the mean intensity of the slave Δy_{Slave} is plotted versus the mean intensity of the master Δy_{Master} for each LED. Fitting a linear function to this data-points, result in the linear correction

$$\Delta y_{Slave} = m \Delta y_{Master} \tag{3.23}$$

with m = 2.04 ± 0.02. Applying this function on the ADC readings of the slave, it results in the corrected data summarized in Table 4.1. With this correction, each LED has a comparable intensity Δy for master and slave. However, this comparison is invalid, as the linear fit for the correction minimizes the differences between master and slave. However, the correction was shown here, as the technic will be similar for calibrating the data of the light sensors if real calibration data will be available in the future.

4 Testing the POCAM in GVD

In the winter of 2016/2017, the first prototype of the POCAM was built for integration in GVD. However, the scope of application for the POCAM should be IceCube, GVD offers surprisingly similar conditions. Therefore the motivation of this experiment was a comprehensive test of hardware, software, and electrics as well as its suitability for calibrating a detector.

For the hardware, the primary goal was to survive the deployment with temperatures to $-20\,°C$ on the frozen lake and a pressure of $\sim100\,bar$ at the final position at $\sim1000\,m$ depth. The challenges for electrics and software are a stable operation at this remote place, where resets or software-updates are nontrivial problems. Last but not least the POCAM needs to trigger several Optical-Modules (OMs) per flash, to make a calibration possible.

During its integration in GVD, the POCAM passed all tests without any problems, and it was possible to trigger hundreds of thousands of events in GVD. Unfortunately, after one year the POCAM had to be dismounted from GVD, because of export limitations in combination with taxes. It was brought back to Munich, where it arrived fully functioning.

The first part of this chapter outlines the deployment, the positioning, and the performed runs. This is followed by an explanation about the needed calibration on the data from the detector and the filter technics to extract the POCAM events. Finally, this chapter will summarize the data analysis of events created by the POCAM.

4.1 Deployment

In March 2017, the deployment took place during the construction phase of the first two clusters of GVD. Before the POCAM was integrated into the detector, it had to pass a communication and a light emission test. The scope of the communication test was a final check if the POCAM works with the detector network. While the second had to verify the order of magnitude of the light emission of a POCAM pulse and if neighboring OMs have to be switched off when the POCAM is flashing. Both tests have been passed, and the light emission was confirmed to be not too strong so that neighboring OMs can stay switched on.

Afterward, the POCAM was integrated into the detector array at string 4, some meters over the communication module of the string. Therefore the position is between the middle and upper section of string 4. The precise location is 5.9 m below the lowest OM of the upper section. Unfortunately,

Figure 4.1: *First water contact of the POCAM during the deployment. For testing the connection to the network of the detector, the POCAM was lowered a bit under the water surface. The modules are directly mounted to the main data cable (black cable) which connects the string communication module with the string center and which can handle loads of anchor and buoy. At the communication module, the load is transferred to a stainless steel cable. The orange data cable connects the next section module with the string communication module. The picture was taken by J. Thompson*

the communication module is also a place where a lot of extra cables has to be stored, which is just ~3 m below the POCAM. Furthermore, the connection cable for the POCAM had to be placed next to the downwards facing hemisphere. Both factors degrade the emission of the downward facing hemisphere. However, as the detector is designed for upwards to horizontal going events, all PMTs are facing downwards. Therefore, the downwards facing hemisphere is less important than the upwards facing hemisphere.

4.2 Raw Data and Data provided by GVD

After a bit more than a month, it was possible to do the first runs with the POCAM and the full operating cluster. A run in GVD is around 10 minutes long and keeps the data of all triggered OMs per event. Besides, it was recommended from GVD to flash the LEDs with a maximum of around 20 Hz. Therefore, the POCAM was flashed in a pattern with various LEDs or combined LEDs to fill the 10 minutes and a rate of 19 Hz. Later this pattern should be found in the data to obtain the configuration. Moreover, this kind of approach was chosen, as the time for the detector was limited and the important configurations of flashing LEDs could be tested.

The raw data provided by GVD consists of an absolute timestamp per event and for every event the time and charge for every triggered OM. The time and charge per OM and event are a result of an algorithm performed by GVD. As the detector digitalize and saves the waveform of every triggered OM per event, the algorithm returns per OM and event the time of the maximum charge and the integral of the total received charge. In addition, GVD provided a geometry and calibration formulas for the detected charge in dependence on charge and direction of the received light.

4.2.1 Data Selection

In total, it was possible to do nine runs with several configurations. From which 4 include a pattern of different LEDs or combined LEDs and 5 with continuously flashing of all LEDs. The later was done to maximize the light emission, as there have been concerns, that the light emitted by the POCAM is too weak for an absorption length of $\sim$20 m.

Unfortunately, the data analysis showed inconsistency when combined LEDs are flashing or with long pulse-lengths of up to 80 ns from the FPGA driven LEDs. The timing distribution of each OM shows two peaks with a separation of $\sim$100 ns and the measured charge seems to be less accurate, even if the signal is stronger but still at least a factor of 2 under saturation. Moreover, the emission of the POCAM was stable during lab tests also with multiple LEDs flashing. Most likely, the reason for the problematic data is the algorithm from GVD which calculates the charge and timing per OM and event, out of the original waveform. It seems, like it randomly triggers between the rising edge or around the middle of the pulse, as a longer FPGA pulse results in more significant separation of the two peaks in the timing distribution. This circumstance makes the analysis much more difficult because the timing of the POCAM is unknown and it has to be determined for every event out of the timing of the surrounding OMs which get less precise with the randomness of the timing.

However, this inconsistency in the data appears only when multiple LEDs are flashing. Therefore, this data has to be excluded from the analysis, which unluckily reduces the data to two runs. Moreover, one of this two includes only very faint events from FPGA driven LEDs with a pulse-length of 10 ns to 40 ns. Conclusively, just one run is left which was also the first run. It contains events of all four LEDs driven by a Kapustinsky circuit. In the following analysis, only this run will be used, which has the run number 49 from GVD.
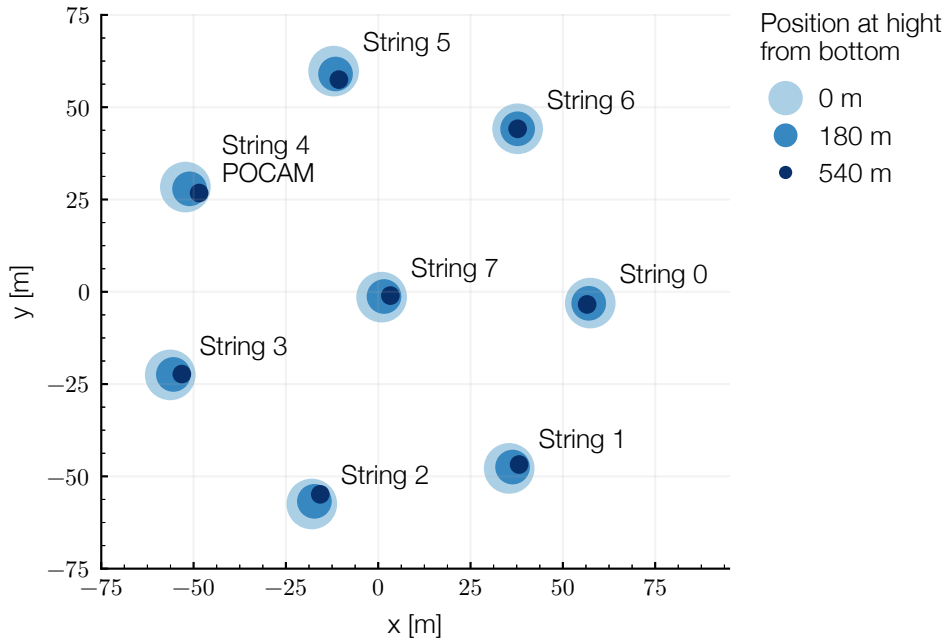
Figure 4.2: *Topview of the detector geometry. Each string is defined by three points at a hight of 0 m, 180 m and 540 m, measured from the lowest OM of the string. To visualize the bending, the three positions for each string are marked with a decreasing size in relation to the hight. Noticeable is string 6, which is perfectly vertical. In other words, it is defined to be like this. The POCAM is placed at string 4 at a hight of 354.3 m.*

4.2.2 Geometry

[tb]

GVD provided a geometry with the position of all OMs in 3D. In a got approximation it is a heptagon with a radius of 60 m and a central string. In Figure 4.2 a topview of it is visualized to show the bending in each string. The position is determined by the know attachment point at the cable and with the help of an acoustic positioning system. Like mentioned in section 2.2, three acoustic modules are attached to each string. One under the lowest OM, another over the highest OM and the last between the lower section and the middle section. By measuring the distance between each acoustic module, the position of each module can be calculated. However, string 6 shows a perfect vertical alignment, which is most likely defined to be like this. Hence, there are strong doubts, that the geometry is very precise.

The POCAM is attached to string 4 between the upper and the middle section. During the deployment, the distance to the module above was measured to be 5.9 m to the vertical center of the POCAM. With the geometry provided by GVD, this results in the coordinates of $x = -49.8$ m, $y = 27.3$ m and $z = 354.3$ m, where the lowest module of the central string 7 is the point of origin.
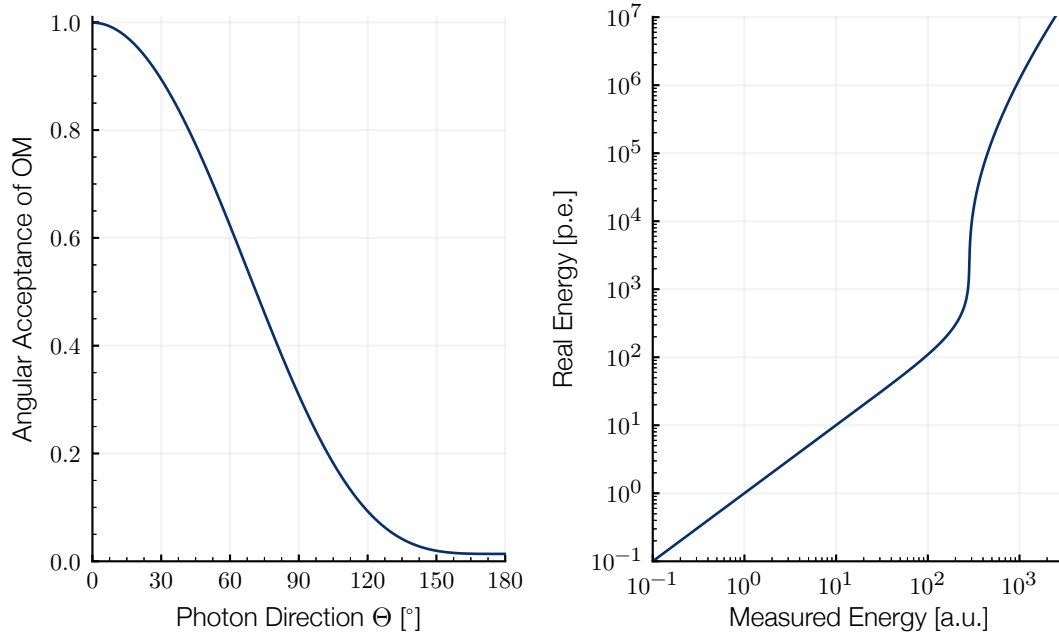
Figure 4.3: *Angular acceptance of the OMs (left) and correction of the energy (right). The angular acceptance gives the ratio of the detected and the actual arriving energy in dependency on the photon direction (Θ = 0° is upwards). The distribution for the energy correction provides a formula to calculate the real energy from the measured energy. The steep part around a measured energy of 200, reflects the saturation of the PMT. Both formulas have to be used for the analysis of the data and have been provided by GVD.*

4.2.3 Energy Calibration

There are two properties which have been taken in to account for the integration of the measured charge of an OM. First the measurement q_m has to be corrected with the angular acceptance $S(\Theta)$ and further with the energy calibration Q_r

$$q_r = Q_r \left(\frac{q_m}{S(\Theta)} \right) \tag{4.1}$$

This calculation has to be done separately for each event, as the direction of the arriving photons are related to the event and therefore has to be included to the fit model. Thankfully, this simplifies for events created by the POCAM, because the direction of the photons is known.

The reason for the angular acceptance is the PMT, as it is covering only the downwards facing part of the surface of an OM. Therefore, the sensitivity is close to 1, for upwards going (Θ = 0°) photons and nearly 0 for downwards going photons. The region in-between can be approximated in first order with the visible area of the PMT under the angel Θ. GVD defined the angular acceptance $S(\Theta)$

of the OMs with a Taylor series

$$S\left(\Theta\right) = \sum_{i=0}^{3} c_i \cos^i\left(\Theta\right) \tag{4.2}$$

where the coefficients are $c_0 = 3082.0 \cdot 10^{-4}$, $c_1 = 5419.2 \cdot 10^{-4}$, $c_2 = 1983.1 \cdot 10^{-4}$ and $c_3 = 491.2 \cdot 10^{-4}$. In Figure 4.3 this function is illustrated.

The energy calibration is provided by GVD with the non-invertible function $Q_m(q_r)$ for the measured charge in dependency on the real charge q_r

$$Q_M\left(q_r\right) = \begin{cases} \dfrac{q_r}{1 + \left|\dfrac{\log_{10}(q_r)}{v_1}\right|^{v_2}} & \text{for} \quad \dfrac{\log_{10}(q_r)}{v_1} \geq 0 \\[4ex] \dfrac{q_r}{1 - \left|\dfrac{\log_{10}(q_r)}{v_1}\right|^{v_2}} & \text{for} \quad \dfrac{\log_{10}(q_r)}{v_1} < 0 \end{cases} \tag{4.3}$$

with $v_1 = 2.681$ and $v_2 = 8.67$. This equation is plotted in Figure 4.3. v_1 determines the charge where the PMT hits its saturation and v_2 characterizes the steepness of the curve when the saturation is reached. Here, a bigger v2 creates a steeper curve when the saturation is reached, but in the original picture of saturation it determines the flatness. If q_r is in the range of

$$-v_1 < \log_{10}(q_r) < v_1 \tag{4.4}$$

it result in

$$\left|\dfrac{\log_{10}(q_r)}{v_1}\right| \ll 1 \quad \text{or} \quad \left|\dfrac{\log_{10}(q_r)}{v_1}\right|^{v_2} \approx 0 \tag{4.5}$$

and $Q_m(q_r)$ can be simplified to

$$Q_M\left(q_r\right) = \dfrac{q_r}{1} = q_r \tag{4.6}$$

and q_m equals q_r. Hence, the real charge is only dependent on the angular acceptance, if the charge is within certain boarders.

However, for the following analysis, this simplification is not done, as the function was inverted numerically and the angles are known for events created by the POCAM anyhow.
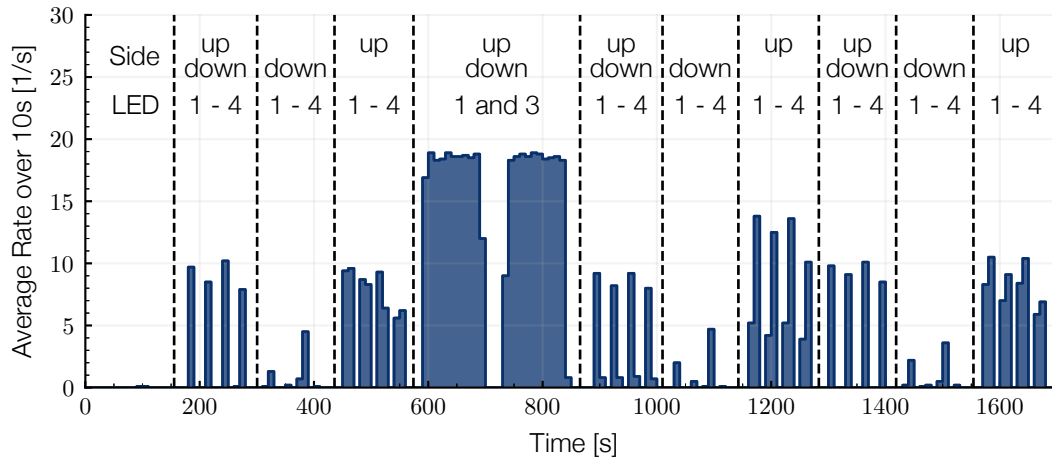
Figure 4.4: *Flashing sequence in run 49. The average rate is calculated with a histogram of the filtered event timestamps with a bin size of 10 s. The flashing sequence is a repetition of three blocks (divided by dashed lines) where each of the four LEDs is flashing simultaneously on both sides and separately. The flashing rate of the POCAM is 19 Hz with a 100 events (up+down, down) and 200 events (down, software bug). Inbetween the two blue LEDs are producing 2000 events each.*

4.3 Filter

The POCAM is integrated into the detectors network but not in the time synchronization or trigger system, therefore, whether the POCAM nor the detector know the events created by the POCAM in the data of a run. Furthermore, the precise timing of the POCAM emission in an event from the POCAM is unknown. Hence, an essential task is to create a filter, which reliably selects only events from the POCAM, also with different flashing configurations.

For a better understanding of the plots shown in this section, first, the sequence of the tested configurations in run 49 is explained. The pattern can be divided into three blocks, which have been repeated three times. In the first block, each of the 4 Kapustinsky driven LEDs is flashing for 100 events simultaneously on both hemispheres. The second block similar to the first, but only the lower hemisphere is flashing. And in the third block, only the upper hemisphere is flashing with 200 events per LED. Here, the 200 have been a software bug of the POCAM. Besides, each of the two blue LEDs (L1 and L3) have been flashed for 2000 events on both hemispheres between the first and second repetition. In Figure 4.4, this pattern is illustrated and labeled.

In run 49, the average background event rate of the detector is around 50 Hz and the POCAM is flashing with 19 Hz. By plotting the average rate in intervals with a size of 10 s, the POCAM should lead to a rise of around 10 Hz ($\approx$ 100 events/10 s), which can be already seen in the unfiltered data of Figure 4.5.

The first filter is a simple trigger on the OM above the POCAM, which is also the closest OM. The idea behind it is that this OM should recognize every emission of the POCAM, even when only the
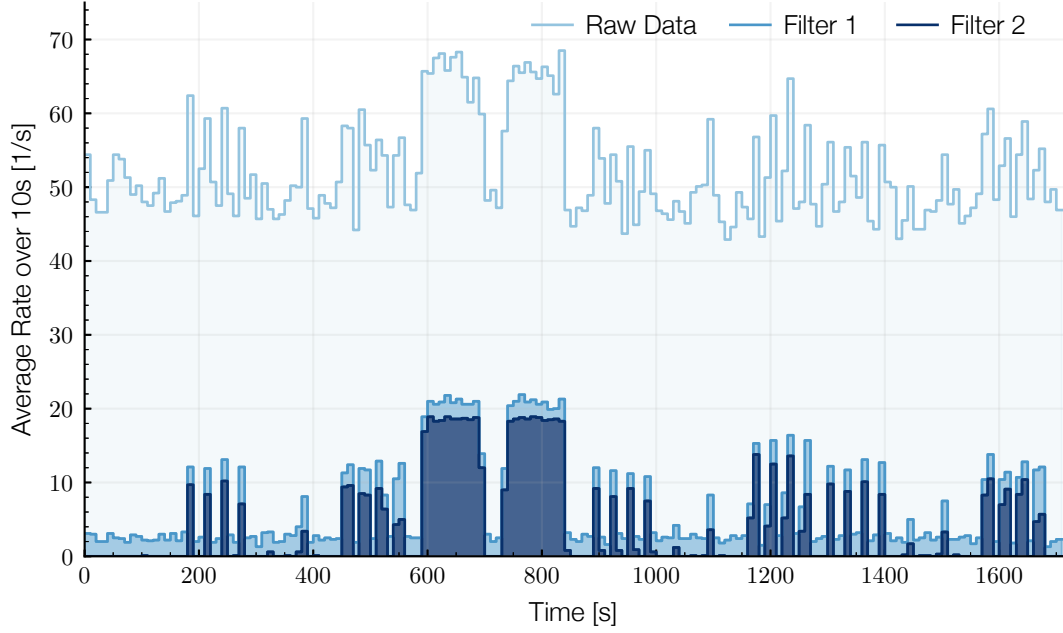
Figure 4.5: *Comparison of the different filter levels. Already in the raw data, the flashing sequence (explained in section 4.3) with a rate of 19 Hz can be recognized over the ~50 Hz background. Triggering on the OM above the POCAM, reduce the background to 3 Hz to 4 Hz. Applying a trigger which also takes the distance of POCAM and OM into account, the background is reduced to 0 Hz. An explanation of the filters can be found in section 4.3.*

lower hemisphere is flashing (down-events). Comparing this with Figure 4.5, the background rate is reduced to 3 Hz to 4 Hz and the configuration pattern of the POCAM is clearly visible, only the rate for the down-events are very low. Because the down-events have additional drawbacks, like the angular acceptance and previously mentioned obstacles close to the POCAM, they will not be used for the further analysis.

The second stage of the filter is counting on triggered OMs with the correct timing. Therefore, the time t_{ij} of each OM_j and event i is normalized with the time value from the OM above the POCAM (OM_{168}).

$$t'_{ij} = t_{ij} - t_{i,168} \tag{4.7}$$

This normalized time t'_{ij} is than converted to a distance d_{ji} with a speed of light in water of 0.22 m/ns ($n \approx 1.36$). Is the distance in a range around the distance r_j from the geometry provided by GVD, the hit will be labeled as a possible hit. The range is defined with 3 % of r_j the plus a constant factor of 2 m.

$$\left| 0.22 \frac{m}{ns} t'_{ij} - r_j \right| \leq 0.03 r_j + 2m \tag{4.8}$$

If now a event has more than 2 possible hits, this event is with nearly 100 % a event created by the POCAM, e.g. Figure 4.5 and Figure 4.4 shows only events which fit in the flashing sequence.

Table 4.1: *Summary of emitted and detected events. The emitted events are the number of flashes from the POCAM, and the detected events are the number of filtered events of the data from GVD.*

LED-ID	Emitted Events			Detected Events			Detection Ratio		
	Up+Down	Up	Down	Up+Down	Up	Down	Up+Down	Up	Down
L1	2300	600	300	2261	568	58	98.3 %	94.7 %	19.3 %
L3	2300	600	300	2259	531	141	98.2 %	88.5 %	47.0 %
L2	300	600	300	266	498	10	88.7 %	83.0 %	3.3 %
L4	300	600	300	251	384	4	90.0 %	64.0 %	1.3 %

Table 4.1 lists the numbers of total emitted events by the POCAM, filtered events, and the filter ratio. The weakness of this filter method is the triggering on OM_{168}, and also, the timing has to be correct. Unfortunately, with a minimal chance, this OM has an incorrect timing or is not triggering at all, even when the signal is far beyond the threshold of 3 p.e. However, this effect is, and this filter will be used for the following data analysis.

Figure 4.6: *Measured speed of light along string 4 where the POCAM is attached. For every event, the speed is fitted at the time of arrival and the distance from the POCAM to the OM. Here, the LEDs are separated by the color blue and green in the right and left plot, respectively.*

4.4 Analysis of the POCAM Events

With the filtered events, some fundamental characteristics of the environment and the detector itself can be analyzed and verified. These characteristics are the wavelength dependent reflective index, the total measured energy and the calibration of the geometry as well as the calculation of the absorption length. For the following examples, only the events created by the POCAM are used in combination with the geometry and the measured time and charge of the detector.

4.4.1 Reflective Index

The calculation of the reflective index of water is based on the time measurements for the distance from POCAM to the OMs. As the exact geometry of the detector is unknown (subsection 4.2.2), only the OMs at the same string, where the POCAM is mounted, will be used. Since the detection range of the light is limited, mainly due to the self-shadowing of the OMs along the string, only the 5 OMs below the POCAM and 8 OMs above are selected for this analysis. To determine the speed of light in water v_i for every event i, the timing t_{ij} of the selected OMs j have to be fitted in dependency on the distance d_{ij} to the POCAM with the equation

$$f_i(t_{ij}) = \frac{t_{ij} - t_{i,\text{POCAM}}}{v_i} \tag{4.9}$$
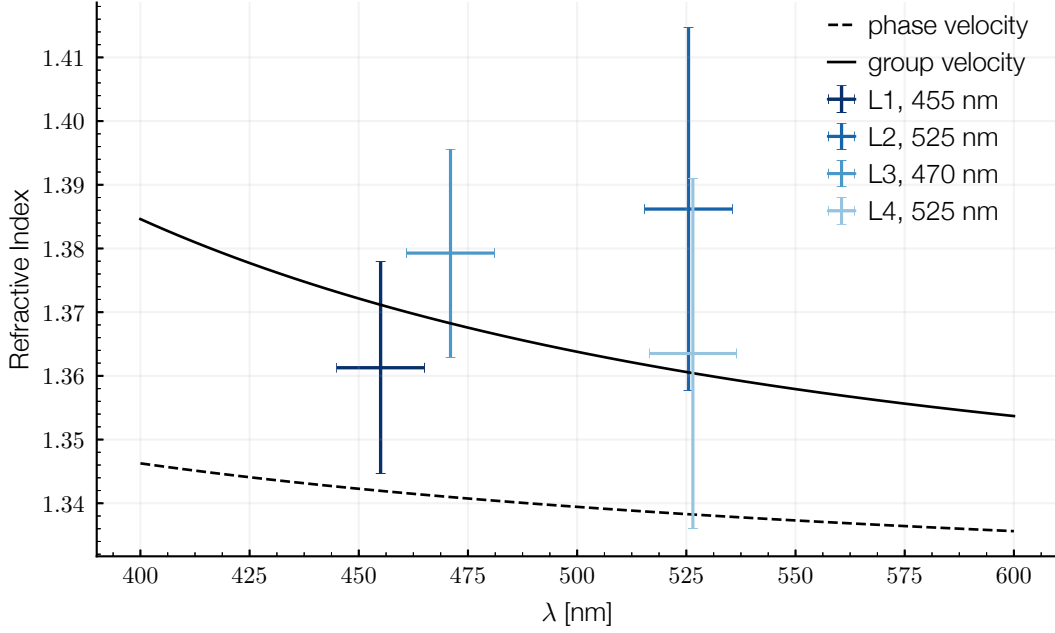
Figure 4.7: *Reflective index in dependence on the wavelength. For each LED the results of the Gaussian fits from Figure 4.6 are plotted with an error of $\Delta x = 10$ nm and Δn is the standard deviation of the Gaussian fit. The phase velocity is defined by eq. (4.14) from the International Association for the Properties of Water and Steam[29]. This phase velocity is transformed in the group velocity by eq. (4.15), which is also the velocity measured by the detector.*

where the offset $t_{i,\text{POCAM}}$ is the time when the POCAM was flashing in the event. Expressing this with the $\mathcal{X}^2$ equation for curve fitting,

$$\mathcal{X}_i^2 = \sum_j \left| d_{ij} - f_i(t_{ij}) \right|^2 \tag{4.10}$$

yield v_i and $t_{i,\text{POCAM}}$ by minimizing $\mathcal{X}_i^2$. As $f_i(t_{ij})$ is a linear function, the variables which are minimizing this problem can be calculated analytically by

$$v_i = \frac{\langle d_{ij} t_{ij} \rangle - \langle d_{ij} \rangle \langle t_{ij} \rangle}{\langle t_{ij}^2 \rangle \langle t_{ij} \rangle^2} \tag{4.11}$$

and

$$t_{i,\text{POCAM}} = \frac{\langle d_{ij} \rangle}{v_i} - \langle t_{ij} \rangle \tag{4.12}$$

where $\langle x_{ij} \rangle$ is the mean per event i of the variable x_{ij} over all triggered OMs j. Here should be mentioned, that d_{ij} can not be simplified to d_j, as it is dependent on the actual triggered OMs per event.

Plotting a histogram of the velocities v_i in dependency on the flashing LED, provides the plot which is illustrated in Figure 4.6. Fitting a Gaussian distribution to the histograms provides the refractive

Table 4.2: *Summary of refractive index and total energy, measured with selected OMs. For the calculation of the reflective index, only the OMs are used, which are mounted on the same string 4 like the POCAM. The total energy is the sum of all OMs attached to strings surrounding string 4 and where the light arrives on the lower hemisphere of the OMs ($\Theta \leq 90°$).*

LED-ID	λ [nm]	refractive index	speed [m/ns]	Total Energy [a.u.]	number events
L1	455	1.361 ± 0.017	220.2 ± 2.7	31.2 ± 8.6	2829
L2	525	1.386 ± 0.028	216.2 ± 4.4	37.1 ± 9.7	764
L3	470	1.379 ± 0.016	217.4 ± 2.6	95.3 ± 14.4	2790
L4	525	1.364 ± 0.028	219.8 ± 4.5	11.0 ± 5.0	635

index and the speed for each LED, which are summarized in Table 4.2 with the total number of events per LED. By plotting this results in dependency on the wavelength of the LEDs, the results can be compared to the optical properties of water from the literature. In Table 4.2 the reference phase velocity is a Taylor series

$$\rho' = \frac{\rho}{\rho_{\text{ref}}} \; ; \qquad T' = \frac{T}{T_{\text{ref}}} \; ; \qquad \lambda' = \frac{\lambda}{\lambda_{\text{ref}}}$$

$$g\left(\rho', T', \lambda'\right) = a_0 + a_1\rho' + a_2 T' + a_3\lambda'^2 T' + \frac{a_4}{\lambda'^2} + \frac{a_5}{\lambda'^2 - \lambda_{uv}^2} + \frac{a6}{\lambda'^2 - \lambda_{ir}^2} + a_7\rho^2 \tag{4.13}$$

$$n_{\text{water}}\left(\rho', T', \lambda'\right) = \sqrt{\frac{2\, g(\rho', T', \lambda') + \rho'^{-1}}{g(\rho', T', \lambda') - \rho'^{-1}}} \tag{4.14}$$

with 13 variables defined by *the International Association for the Properties of Water and Steam* from 1997. [29]

Because the detector is measuring the group velocity n_g, n_g has to calculated with

$$n_g = \frac{1}{n - \lambda\frac{dn}{d\lambda}} \qquad ; \text{with } n_{\text{water}}\left(\rho', T', \lambda'\right) = n \tag{4.15}$$

which is also plotted in Table 4.2. Therefore, the measurements provide a comparable result to the literature within the uncertainties.

4.4.2 Energy

One of the fundamental motivations for the POCAM is the calibration of the total measured charge from the detector. The POCAM has an in-situ calibrated device; hence the emitted charge is known relatively between different LEDs or different pulse length of the FPGA. For this POCAM it does not hold in an absolute sense, as this POCAM was the first prototype and an absolute calibration was not possible due to time limitation. Therefore, the only comparison is possible for the total emitted charge and the total detected charge. In Figure 4.8, this comparison is illustrated for the four Kapustinsky
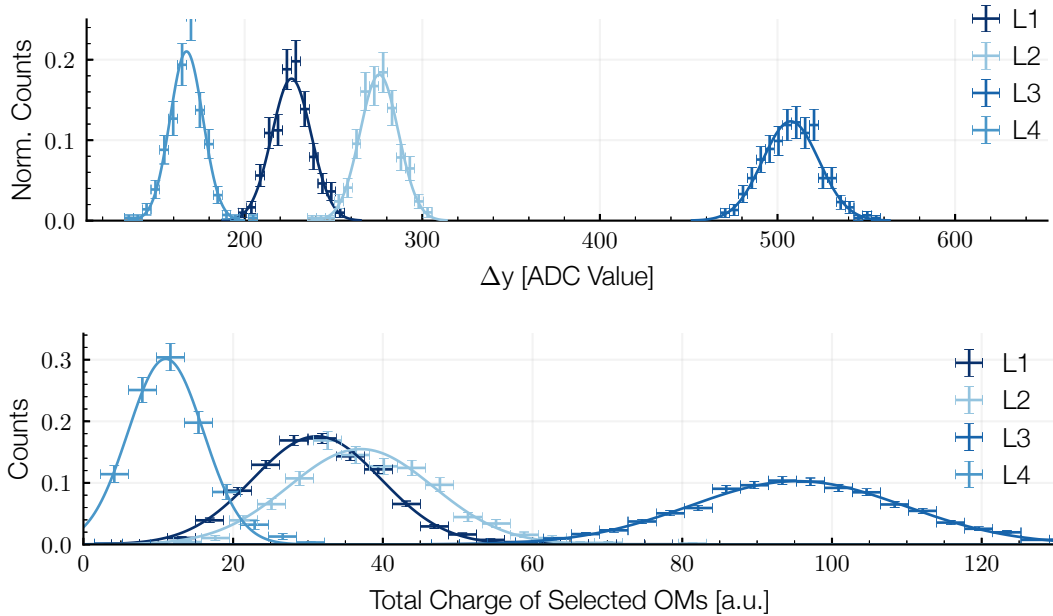
Figure 4.8: *Comparison of emitted charge by the POCAM and the measured charge of the detector. At the upper plot, the charge, measured by the internal SiPM of the POCAM, is plotted for the four Kapustinsky driven LEDs. At the lower plot, the distribution of the total energy, detected by the OMs at the surrounding strings (3,5,7), are illustrated. In both plots the order is similar for the brightness of the LEDs. Moreover, there could be a linear correlation of the positions of the peaks in both data sets.*

driven LEDs. The total detected charge is the sum of triggered OMs per event. Here, only the OMs are used, which are mounted at the three closest strings to the string where the POCAM is mounted. Furthermore, only the OMs are taken into account, where the light of the POCAM hits the lower hemisphere. In other words, the z-component (hight) has to be greater than the z-component of the POCAM, as otherwise, the correction of the angular acceptance is increasing the error.

First of all, the order in the brightness is similar for the LEDs in both data sets. Furthermore, the distribution for each LED gets wider in the data from the detector. And there could be a linear correlation between the position of the peaks from the monitoring sensors and the detector data. In Table 4.2 the fit results are summarized for the energy distributions measured by the detector. For a comparison to the data from other LEDs see Figure A.3, Figure A.5.

4.4.3 Geometry

With the help of the POCAM also the geometry can be verified or calibrated. Therefore, the runtime is measured from the moment when the POCAM is emitting a light pulse until the OMs recognize the flash. Unfortunately, the timing of the POCAM pulse is unknown, as the POCAM is not connected
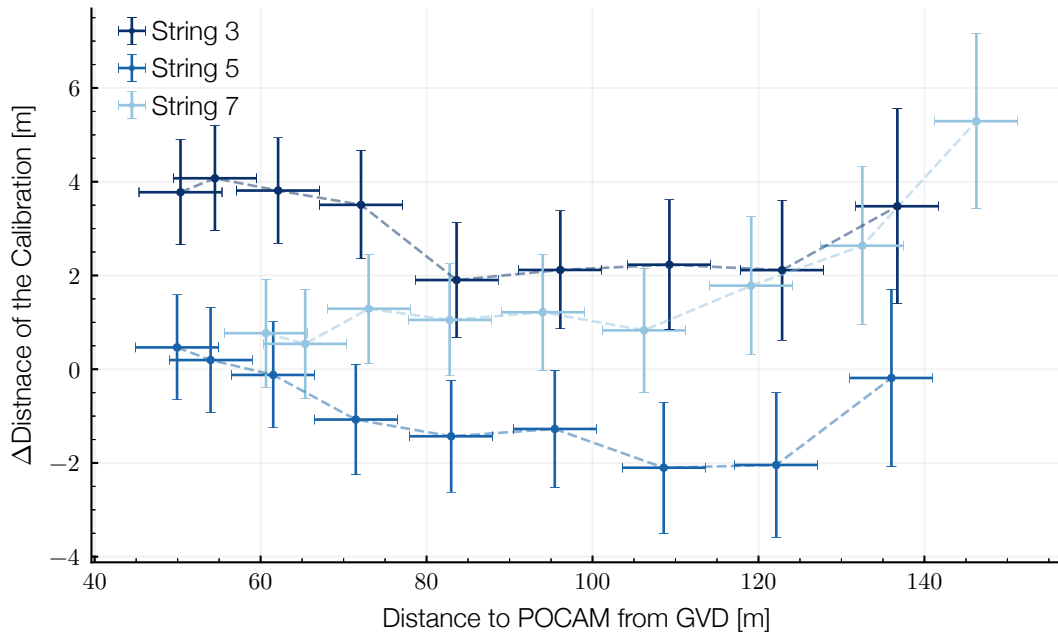
Figure 4.9: *Difference in the geometry from GVD and the calibration with the POCAM. The Δdistance is the difference between the distances from each OM to the POCAM, calculated by the geometry provided by GVD and the runtime measurements from POCAM events with LED L3. As the differences are not varying a lot for neighboring OMs on a string and the updated distances yield a more consistent distribution of the absorption length, this calibration seems to work. However, a crosscheck with a second instrument, e.g., an additional POCAM, is desirable.*

to the time synchronization of the detector. To determine the timing, the eq. (4.12) can be used in combination with the OMs next to the POCAM and which are attached to the same string. Selecting the OM in this way has the advantage, that the vertical position along the string is known quite precisely. With the known timing of the POCAM, the calculation of the distances is straightforward, by dividing the mean Δt of each OM with the speed of light in water. For the speed, the results from subsection 4.4.1 can be used, which are around 0.218 m/ns.

To determine the quality of the calibration, the difference in distance is plotted for the geometry provided by GVD and measurements with LED L3 from the POCAM, in Figure 4.9. As the differences are in a range from –2 m to 5 m and the OMs of a single string are in a range of ±2 m, the results are promising for the calibrated distances. However, a crosscheck with a different module or even an additional POCAM would be desirable. For a comparison to the data form other LEDs see Figure A.4 and Figure A.3.
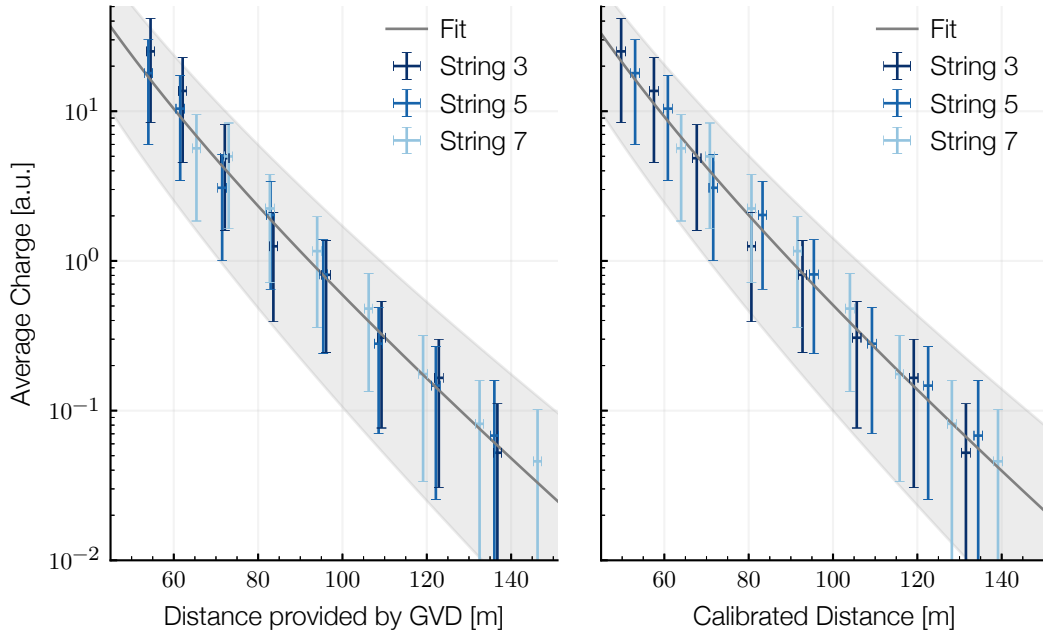
Figure 4.10: *Comparison of calibrated and provided geometry at the attenuation length. Both plots show the average charge per OM of events created by the POCAM with LED L3. The difference is the distances of each OM. On the left, the distance is calculated from the geometry provided by GVD. And on the right, the calibrated distances are the result of the runtime measurements of the same events which provide the average charge. With the calibrated distances, the data-points align more, especially for a higher charge and also the $\sum \mathcal{X}^2$ reduced.*

4.4.4 Attenuation Length

The attenuation length is an important criterion for the energy reconstruction of events in a detector like GVD. It determines the loss of energy per length for the light traveling through the media. In dependence on the media of the detector, also the scattering length is an important criterion, as it extends the traveling length of the light from the event to the OMs. However, measurements showed that the attenuation length is dominant with $\sim 20\,\text{m}$ in comparison to the scattering length of $30\,\text{m}$ to $50\,\text{m}$ in the water of Lake Baikal. [3]

One way to calculate the attenuation length in a detector array is to measure the energy in dependency on the distance. The isotropy of the POCAM simplifies this measurement a lot, as no angular dependency of the initial event has to be considered. Besides, this allows using multiple OMs in all directions, which reduce the effect on the calculation created by uncertainties from single OMs. Nevertheless, the angular acceptance of the OMs limits the number of OMs for the analysis, as they are only sensitive to light arriving from below. In the following calculation, only the OMs are taken into account where the light enters horizontally or from below.

From the *Beer–Lambert* law, the intensity I is expressed in dependency on the propagated distance

through a medium r by a decay function

$$I(r) = I_0\, e^{-\frac{r}{\tau}} \tag{4.16}$$

where I_0 is the initial intensity and τ is the attenuation length. Furthermore, the expanding surface of the light pulse has to be taken into account

$$I(r) = I_0\, e^{-\frac{r}{\tau}}\, \frac{A_0}{A(r)} \tag{4.17}$$

with A_0 and $A(r)$ are the initial beam surface and the surface at the distance r. Because it is an isotropic emission, $A(r)$ is the surface of a sphere with radius r. The OMs are measuring the integrated charge of arriving photons, and the sensitive area of all OMs is normalized with the angular acceptance. Hence, the intensity is proportional to the charge q

$$I(r) \sim q(r) \tag{4.18}$$

and the measured charge q_j is

$$q_j = Q_0\, \frac{1m^2}{4\pi r_j^2}\, e^{-\frac{r_j}{\tau}} \tag{4.19}$$

at the OM j with the distance r_j to the POCAM and Q_0 is the initial charge.

To calculate the average charge per OM, the distributions of the charge have to be analyzed. If the average arriving charge is big enough, the distribution can be expressed by a Gaussian function. But when the signal is getting weaker for longer distances, the detection rate of is reduced significantly, as PMT has a detection efficiency and the electronic can fail to trigger. This is leading to a Poisson distribution where the untriggered events are set to a charge of 0. In both cases, the fitted charge is similar to the average charge where untriggered events are counted with a charge of 0.

Concerning the distances of the OMs, here two different set of data can be used. One is the distance calculated from the geometry provided by GVD, and the other is to use the runtime measurements of the same events which provide the charge. For both set of distances the best fit values are summarized with the $\sum \mathcal{X}^2$ at the minimum in Table 4.3 and for L3 they are plotted In Figure 4.10. By comparing the results of both set of distances, the calibrated distance reduce the $\sum \mathcal{X}^2$ for every LED. This can also be recognized in Figure 4.10, where that average charge of the OMs match better to the calibrated distances, as it aligns the data-points more precisely. However, this is not a proof that the calibrated distance is more precise than the geometry from GVD.

Table 4.3: *Best fit results of the attenuation length (att. length) for the calibrated and provided geometry.*

LED-ID	λ [nm]	Geometry from GVD			Calibrated Geometry		
		att. length [m]	Q_0 [10^6 a.u.]	$\sum \mathcal{X}^2$	att. length [m]	Q_0 [10^6a.u.]	$\sum \mathcal{X}^2$
L1	455	21.9 ± 4.1	2.4 ± 1.7	2.00	21.7 ± 3.9	2.3 ± 1.6	1.48
L2	525	23.0 ± 4.7	2.5 ± 1.9	2.17	21.8 ± 4.0	3.2 ± 2.3	1.54
L3	470	21.7 ± 3.2	7.4 ± 4.5	2.08	21.3 ± 3.0	6.9 ± 4.0	1.67
L4	525	24.7 ± 8.2	7.0 ± 7.3	1.58	22.4 ± 6.8	1.3 ± 1.4	1.09

5 Conclusion

Designed initially for IceCube, the opportunity to test the POCAM in GVD triggered improvements on multiple levels. In this thesis, the development and the prototype itself is presented. The software and hardware had to be designed for continuous and stable operation, as a failure cannot be repaired after the deployment. During the development, the primary challenge was to achieve isotropic light emission in 4π. The pressure housing is an exclusive design, where a titanium cylinder separates two glass hemispheres. Moreover, the diffuser is a sphere machined nearly in one piece out of PTFE.

At the time of integration, several thousands of events have been triggered. This thesis analyzes these events by using the data from the detector and the in-situ monitoring of the POCAM. The data provided by GVD have been limited to two calibration curves, a 3D geometry of the detector and an absolute timestamp per event as well as single values for charge and time per Optical Module (OM) and event. Besides, long pulses from the POCAM result in inconsistent data from the detector. Moreover, the POCAM was integrated to the detector as a stand-alone module only connected to the network for the slow control. Therefore, no event-flag or precise timing of the POCAM is known. To select the events an effective filter had to be created. With it, it was possible to verify several properties of the water and the detector. A previous measurements of the attenuation length and the reflective index can be confirmed with $(21 \pm 4)\,\mathrm{m}$[3] and 1.38 ± 0.02[29] , respectively. The geometry calculated from the runtime seems to be more precise than the geometry provided by GVD. Also, the detected total charge of GVD seams to be proportional to charge measured in-situ. For more established statements, several POCAM have to be integrated with more created events and better insight to GVD.

After one year of integration in GVD, the POCAM was recovered, and it arrived fully functioning in Munich. Since June 2018, three POCAMs have been deployed safely with the STRAW project in the Pacific Ocean at a depth of $2600\,\mathrm{m}$. With this tests, the POCAM showed its suitability for extreme environments and qualification to use it for calibration. In the meantime, many improvements have been made, and the list of ideas is not finished yet. The primary attention will be to increase the isotropy in 4π and to specify the emission with lower uncertainty.

A Additional Plots and Summary
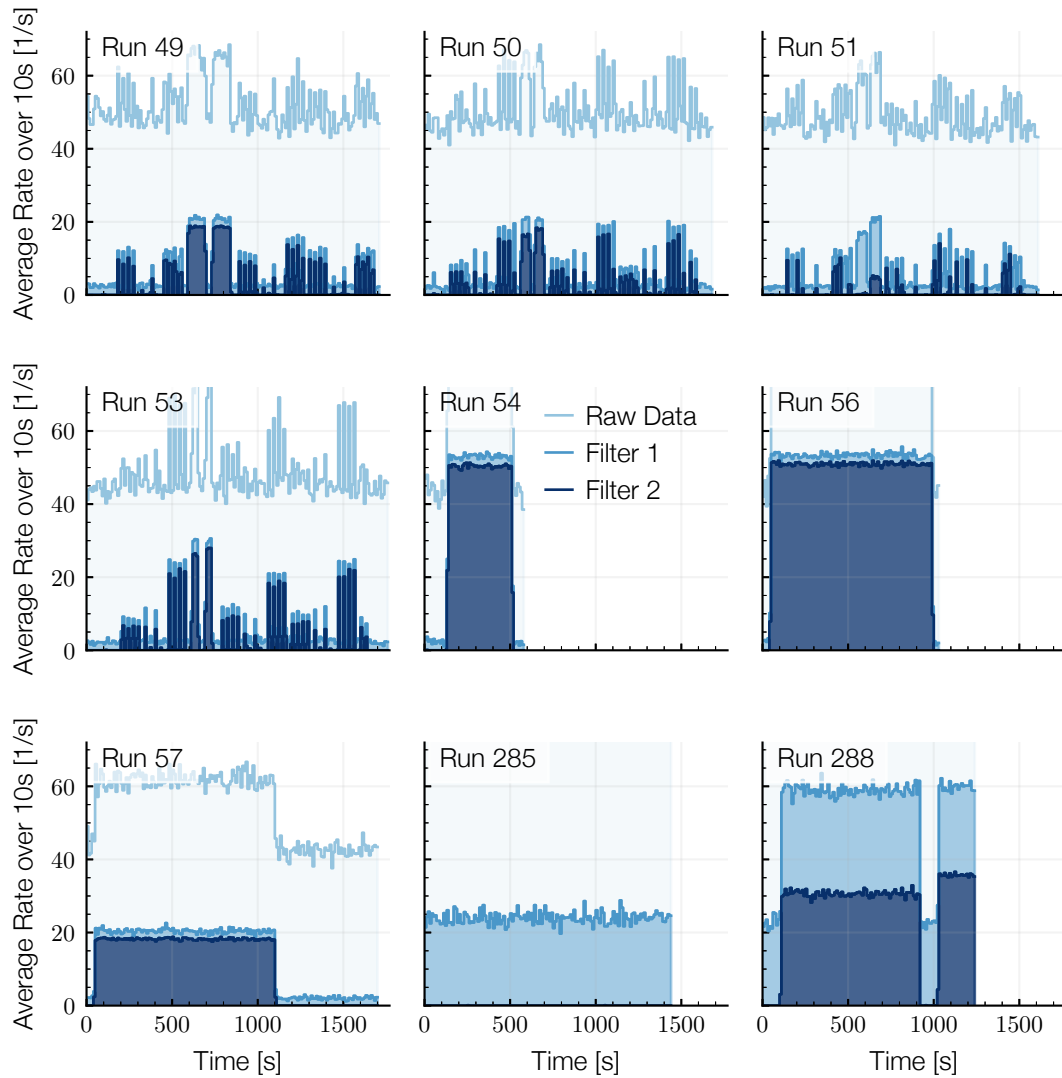
Figure A.1: *Comparison of the different filter levels for all runs (see section 4.3). The total number of detected and emitted event is summarized in Table A.1.*
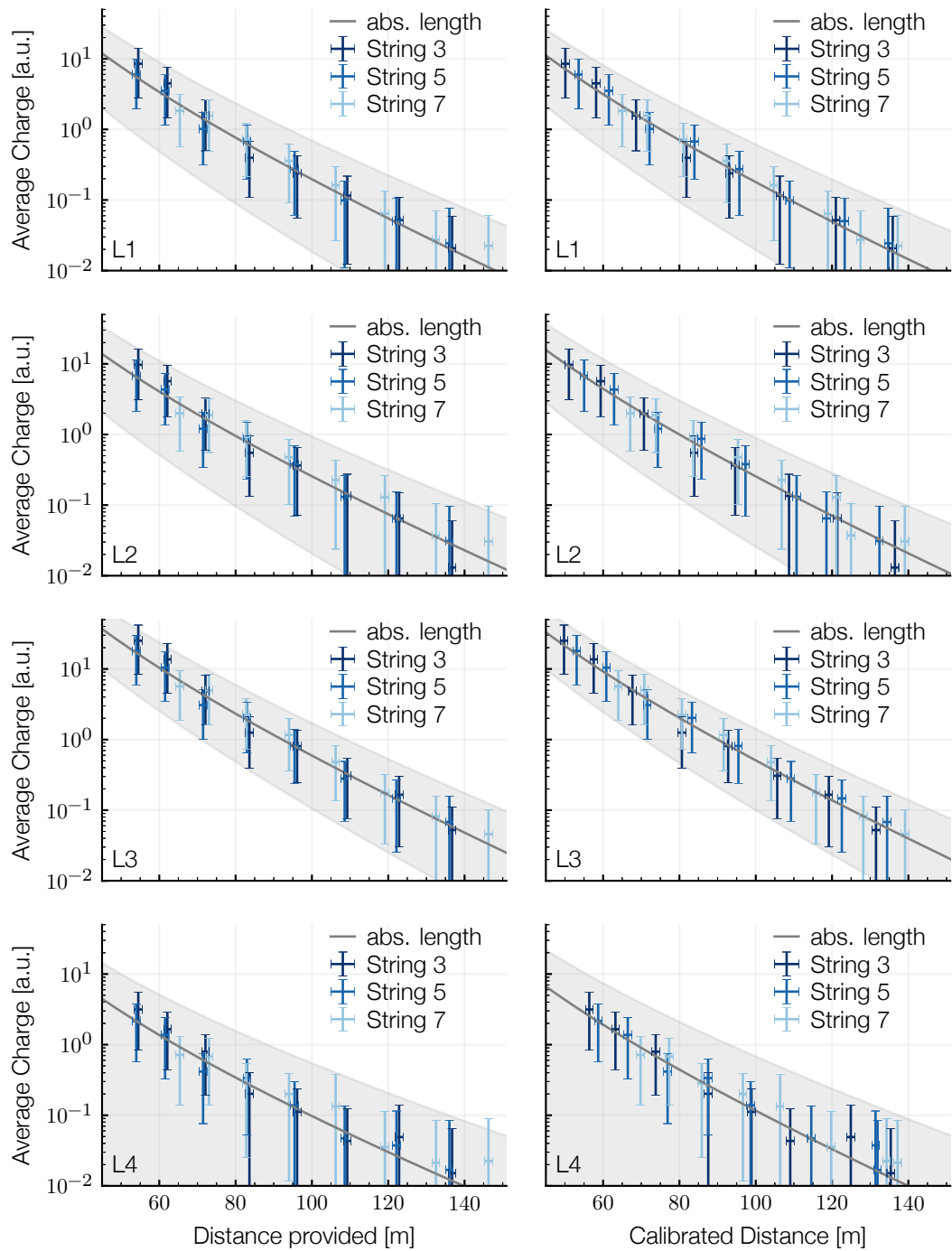
Figure A.2: *The fit of the attenuation length in comparison of the calibrated and provided geometry for all LEDs in run 49 (see subsection 4.4.4). The best fit values are summarized in Table A.1*
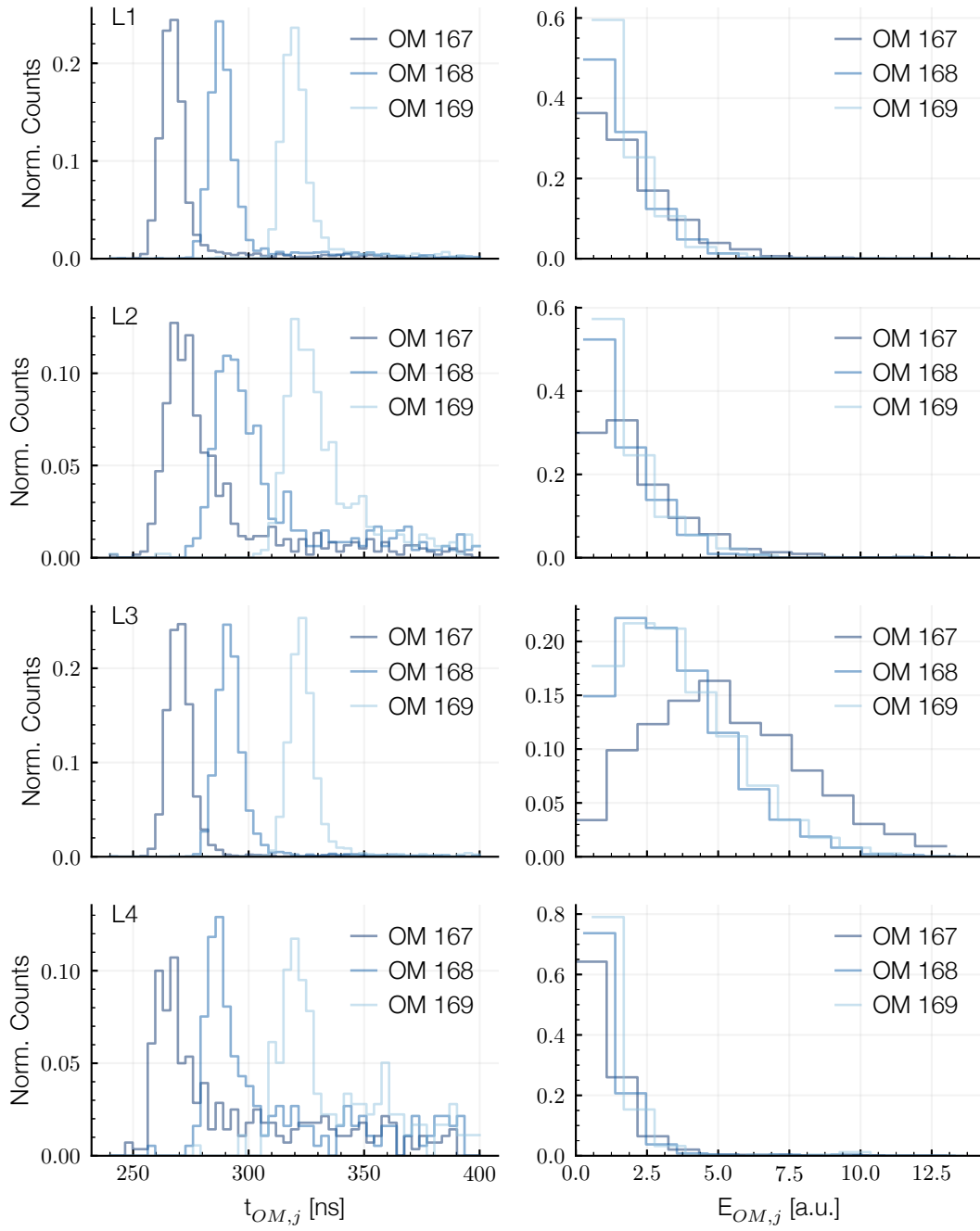
Figure A.3: *Arrival Time and Energy per OM for L1-L4 . OM 168, OM 169, OM 170 are the OMs above the POCAM, respectively.*
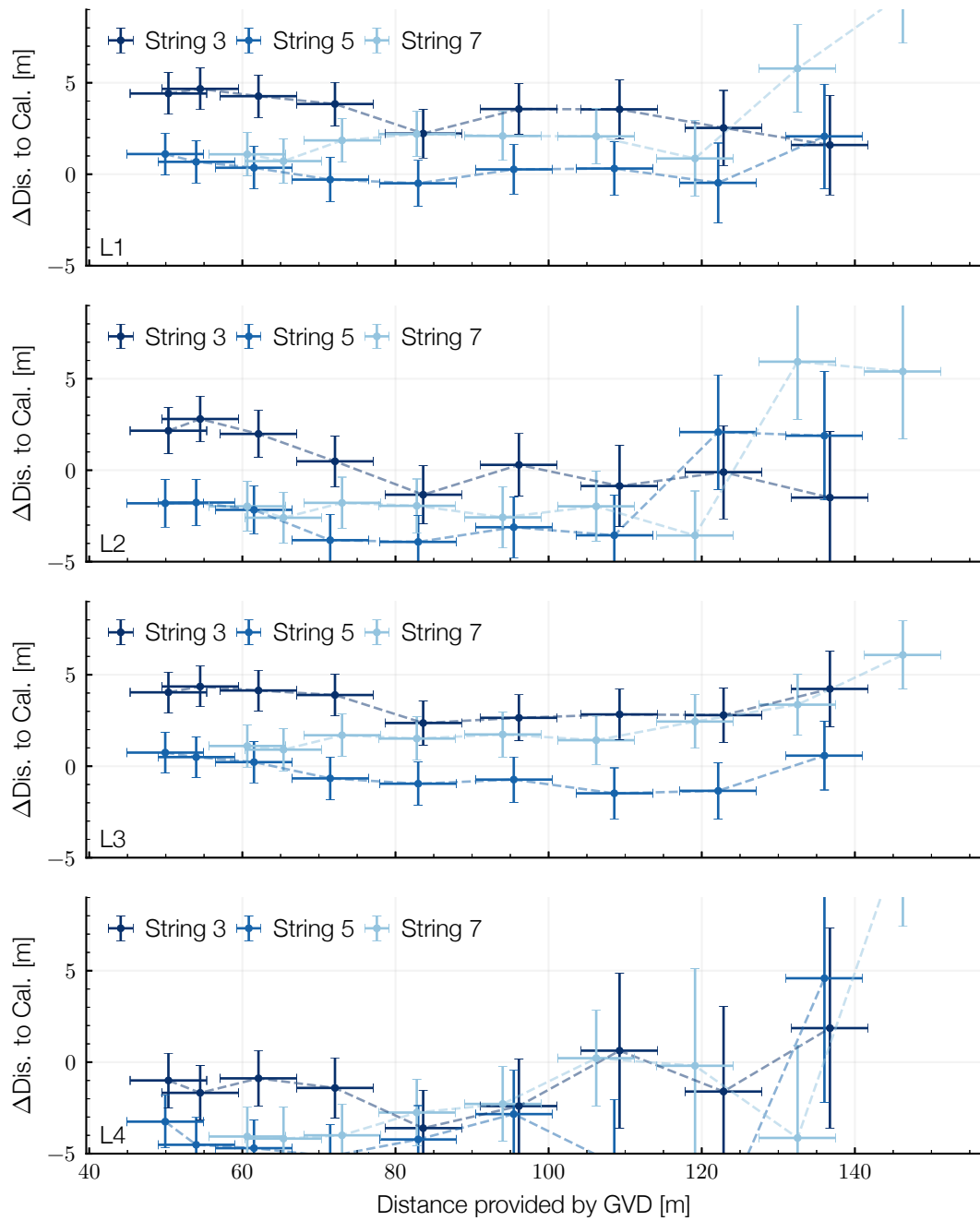
Figure A.4: *Comparison of calibrated and provided geometry for all LEDs in run 49 (see subsection 4.4.3. L2 and L4 result in inconsistent values, as the intensity is low.*
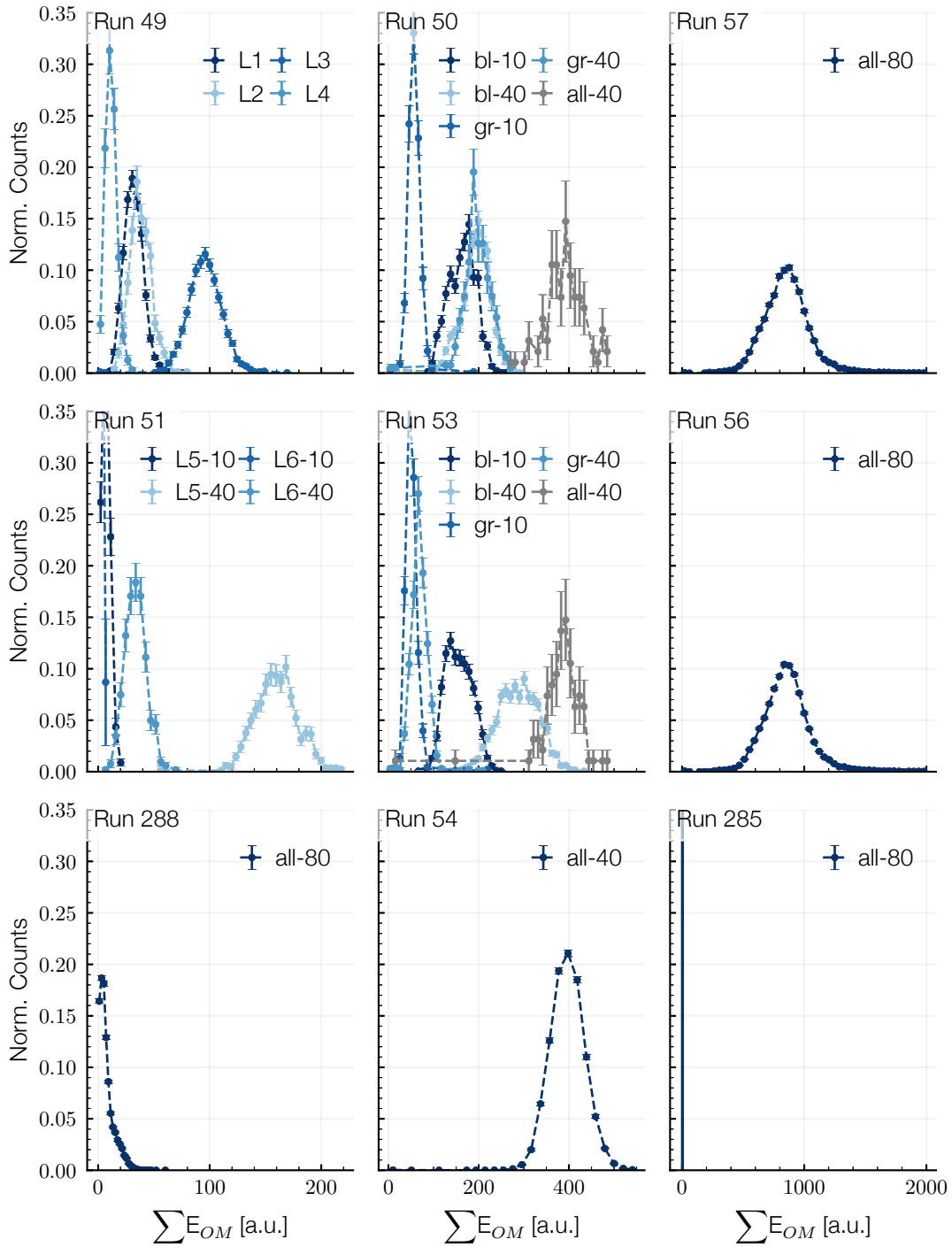
Figure A.5: *Total energy of selected OMs per Event (see. subsection 4.4.2). The best fit values from a Gaussian fit are summarized in Table A.1.*

Table A.1: *Best fit parameters for all runs and all LEDs.*

Run	LED	t_{FPGA}	Events	Detected	abs. length	E_0 [10^6a.u.]	E_{sum} [a.u.]
49	1	–	2900	2829	21.6 ± 3.9	2.2 ± 1.6	32 ± 8
	2	–	900	764	22.1 ± 4.1	3.2 ± 2.3	38 ± 9
	3	–	2900	2790	21.5 ± 3.0	7.0 ± 4.1	96 ± 15
	4	–	900	635	22.4 ± 6.8	1.2 ± 1.4	11 ± 5
50	1,3,5	10 ns	2900	1633	20.4 ± 2.6	14.1 ± 7.9	164 ± 29
	1,3,5	40 ns	2900	1776	21.3 ± 2.6	14.9 ± 7.9	195 ± 29
	2,4,6	10 ns	900	793	22.7 ± 3.9	4.6 ± 3.1	57 ± 12
	2,4,6	40 ns	900	389	14.8 ± 1.8	376 ± 318	199 ± 28
	1-6	40 ns	100	95	21.2 ± 2.7	44.5 ± 25.5	392 ± 40
51	5	10 ns	2900	688	22.9 ± 8.3	0.5 ± 0.5	7 ± 4
	5	40 ns	2900	828	21.1 ± 2.8	15.8 ± 9.3	160 ± 18
	6	10 ns	900	23	fit failed	fit failed	fit failed
	6	40 ns	900	522	22.0 ± 4.9	3.5 ± 3.1	33 ± 9
53	1,3,5	10 ns	2900	1802	21.6 ± 2.9	10.8 ± 6.1	158 ± 28
	1,3,5	40 ns	2900	1927	19.2 ± 1.9	52.8 ± 26.9	287 ± 45
	2,4,6	10 ns	900	882	22.9 ± 4.2	3.6 ± 2.5	50 ± 11
	2,4,6	40 ns	900	948	21.0 ± 3.3	8.6 ± 6.0	69 ± 16
	1-6	40 ns	100	95	20.1 ± 2.4	51.2 ± 29.0	387 ± 30
54	1-6	40 ns	20000	19025	18.5 ± 1.5	74.8 ± 34.8	397 ± 38
56	1-6	80 ns	50000	48073	15.2 ± 1.1	429 ± 229	845 ± 166
57	1-6	80 ns	20000	19179	15.1 ± 1.1	435 ± 235	846 ± 168
285	1-6	80 ns	50000	2	fit failed	fit failed	fit failed
288	1-6	80 ns	50000	32594	fit failed	fit failed	fit failed

Bibliography

[1] M. Ackermann et al. "Optical properties of deep glacial ice at the South Pole". In: *Journal of Geophysical Research: Atmospheres* 111.D13 (). eprint: `https://agupubs.onlinelibrary.wiley.com/doi/pdf/10.1029/2005JD006687`.

[2] E. Kh. Akhmedov. "Parametric resonance of neutrino oscillations and passage of solar and atmospheric neutrinos through the earth". In: (1998). eprint: `arXiv:hep-ph/9805272`.

[3] A. D. Avrorin et al. "Status and recent results of the BAIKAL-GVD project". In: *Phys. Part. Nucl.* 46.2 (2015), pp. 211–221.

[4] A. D. Avrorin et al. "The prototyping/early construction phase of the BAIKAL-GVD project". In: (2013). eprint: `arXiv:1308.1833`.

[5] A. V. Avrorin et al. "Data acquisition system for the Baikal-GVD neutrino telescope". In: *Phys. Part. Nucl.* 47.6 (2016), pp. 933–937.

[6] V. Aynutdinov et al. "The BAIKAL neutrino experiment: From NT200 to NT200+". In: *Nuclear Instruments and Methods in Physics Research Section A: Accelerators, Spectrometers, Detectors and Associated Equipment* 567.2 (2006). VLVnT2, pp. 433–437.

[7] V.A. Balkanov et al. "The Baikal deep Underwater Neutrino Experiment: Results, status, future". In: *Progress in Particle and Nuclear Physics* 40 (1998). Neutrinos in Astro, Particle and Nuclear Physics, pp. 391–401.

[8] Carsten Burgard. *Example: Standard model of physics*. 2016. url: `http://www.texample.net/tikz/examples/model-physics/` (visited on 08/04/2018).

[9] B. T. Cleveland et al. "Measurement of the solar electron neutrino flux with the Homestake chlorine detector". In: *Astrophys. J.* 496 (1998), pp. 505–526.

[10] DONUT Collaboration. "Observation of Tau Neutrino Interactions". In: (2000). eprint: `arXiv:hep-ex/0012035`.

[11] IceCube-Gen2 Collaboration et al. *IceCube-Gen2: A Vision for the Future of Neutrino Astronomy in Antarctica*. 2014. eprint: `arXiv:1412.5106`.

[12] The IceCube-PINGU Collaboration. *Letter of Intent: The Precision IceCube Next Generation Upgrade (PINGU)*. 2014. eprint: `arXiv:1401.2046`.

[13] *CR-110-R2 charge sensitive preamplifier: application guide*. CR-110-R2.1. Rev. 2. Cremat Inc. Oct. 2018.

[14] *CR-113-R2.1 charge sensitive preamplifier: application guide*. CR-113-R2.1. Rev. 2.1. Cremat Inc. Oct. 2018.

[15] Thomas K. Gaisser, Ralph Engel, and Elisa Resconi. *Cosmic Rays and Particle Physics*. 2nd ed. Cambridge University Press, 2016.

[16] Carlo Giunti. *Fundamentals of neutrino physics and astrophysics*. Oxford: Oxford University Press, 2007.

Bibliography

[17] Felix Henningsen. "Optical Characterization of the Deep Pacific Ocean: Development of an Optical Sensor Array for a Future Neutrino Telescope". MA thesis. Munich, Tech. U., 2018.

[18] Deborah Hutchinson and Steve and Colman. "Lake Baikal— A Touchstone for Global Change and Rift Studies". In: *Water Encyclopedia*. American Cancer Society, 2005, pp. 20–22. eprint: `https://onlinelibrary.wiley.com/doi/pdf/10.1002/047147844X.sw2165`.

[19] The IceCube et al. "Multi-messenger observations of a flaring blazar coincident with high-energy neutrino IceCube-170922A". In: (2018). eprint: `arXiv:1807.08816`.

[20] J Jung et al. "Diel vertical migration of zooplankton in Lake Baikal and its relationship to body size". In: *Ecosystems and Natural Resources of Mountain Regions. Novosibirsk, Russia* (2004), pp. 131–140.

[21] Kara M. Merfeld and David C. Latimer. "Parametric enhancement of flavor oscillation in a three-neutrino framework". In: (2014). eprint: `arXiv:1412.2728`.

[22] Spandan Mondal. *Physics of Neutrino Oscillation*. 2015. eprint: `arXiv:1511.06752`.

[23] C. Patrignani et al. "Review of Particle Physics". In: *Chin. Phys.* C40.10 (2016), p. 100001.

[24] B. Pontecorvo. "Mesonium and anti-mesonium". In: *Sov. Phys. JETP* 6 (1957). [Zh. Eksp. Teor. Fiz.33,549(1957)], p. 429.

[25] A. D. Sakharov. "Violation of CP Invariance, C asymmetry, and baryon asymmetry of the universe". In: *Pisma Zh. Eksp. Teor. Fiz.* 5 (1967). [Usp. Fiz. Nauk161,no.5,61(1991)], pp. 32–35.

[26] Christine Sutton. *Spaceship Neutrino*. 1st ed. Cambridge University Press, Oct. 1992.

[27] Jennifer A Thomas and Patricia L Vahle. *Neutrino Oscillations*. WORLD SCIENTIFIC, 2008. eprint: `https://www.worldscientific.com/doi/pdf/10.1142/6615`.

[28] Paul A. Tipler and Ralph Llewellyn. *Modern Physics*. 5th. W. H. Freeman, Sept. 2007.

[29] W. Wagner et al. "The IAPWS Industrial Formulation 1997 for the Thermodynamic Properties of Water and Steam". In: *Journal of Engineering for Gas Turbines and Power* 122.1 (2000), pp. 150–184.

[30] R. Wischnewski and for the Baikal Collaboration. "The Baikal Neutrino Telescope - Results and Plans". In: (2005). eprint: `arXiv:astro-ph/0507698`.